Optimality-Based Non-Redfield Plankton-Ecosystem Model (OPEM v1.0) in the UVic-ESCM 2.9. Part I: Implementation and Model Behaviour

Markus Pahlow[1], Chia-Te Chien[1], Lionel Alejandro Arteaga[2], and Andreas Oschlies[1]

[1]GEOMAR Helmholtz Centre for Ocean Research Kiel, Düsternbrooker Weg 20, 24105 Kiel, Germany
[2]Princeton University, Princeton, NJ, USA

Correspondence: M. Pahlow (mpahlow@geomar.de)

Abstract.

Uncertainties in projections of marine biogeochemistry from Earth system models (ESMs) are associated to a large degree with the imperfect representation of the marine plankton ecosystem, in particular the physiology of primary and secondary producers. Here we describe the implementation of an optimality-based plankton-ecosystem model (OPEM) version 1.0 with

5 variable C:N:P stoichiometry in the University of Victoria ESM (UVic) and the behaviour of two calibrated reference configurations, which differ in the assumed temperature dependence of diazotrophs.

Predicted tracer distributions of oxygen and dissolved inorganic nutrients are similar to those of an earlier fixed-stoichiometry model (Keller et al., 2012). Compared to the classic fixed-stoichiometry model, OPEM is closer to recent satellite-based estimates of net community production (NCP), despite overestimating net primary production (NPP), can better reproduce

10 deep-ocean gradients in the NO_3^-:PO_4^{3-} ratio, and partially explains observed patterns of particulate C:N:P in the surface ocean. Allowing diazotrophs to grow (but not necessarily fix N_2) at similar temperatures as other phytoplankton results in a better representation of surface Chl and NPP in the Arctic and Antarctic Oceans.

Deficiencies of our calibrated OPEM configurations may serve as a magnifying glass for shortcomings in global biogeochemical models and hence guide future model development. The overestimation of NPP at low latitudes indicates the

15 need for improved representations of temperature effects on biotic processes, as well as phytoplankton community composition, which may be represented by locally-varying parameters based on suitable trade-offs. Discrepancies between observed and predicted vertical gradients in particulate C:N:P ratios suggest the need to include preferential P remineralisation, which could also benefit the representation of N_2 fixation. While OPEM yields a much improved distribution of surface N* ($NO_3^- - 16 \cdot PO_4^{3-} + 2.9\,\mathrm{mmol\,m^{-3}}$), it still fails to reproduce observed N* in the Arctic, possibly related to a mis-representation

20 of the phytoplankton community there and the lack of benthic denitrification in the model. Coexisting ordinary and diazotrophic phytoplankton can exert strong control on N* in our simulations, which questions the interpretation of N* as reflecting the balance of N_2 fixation and denitrification.

Geoscientific
Model Development
Discussions

1 Introduction

25 Earth system models (ESMs) are routinely used for simulating both the possible future development and the past of our climate system (e.g. IPCC, 2013; Hülse et al., 2017; Keller et al., 2018; Park et al., 2019). While different ESMs agree to some extent in their predictions, they usually also encompass a rather wide range, e.g., in the predicted temperature increase until the end of the current century (IPCC, 2013). Some predictions do not even agree in the sign of the projected changes, e.g., of marine net primary production, particularly in low latitudes, varying between −25 % and 40 % across current models (Laufkötter et al.,

30 2015; see also Taucher and Oschlies, 2011). But even where many ESMs agree, their predictions are sometimes counter to observations, e.g., in the case of oceanic O_2 patterns and trends (Oschlies et al., 2017). These problems are likely rooted in uncertainties in parameter estimates (Löptien and Dietze, 2017) but also inherent model deficiencies, such as limited spatio-temporal resolution or inaccurate representation of physical and biotic processes (Keller et al., 2012; Getzlaff and Dietze, 2013).

35 In our view, a major limitation of the biogeochemical modules of current ESMs is that the formulations used to describe the plankton compartments are at odds with organism behaviour as observed in the laboratory. While the variability of the chlorophyll:carbon (Chl:C) ratio is considered in recent ESMs (e.g., Park et al., 2019), the carbon:nitrogen:phosphorus (C:N:P) stoichiometry of phytoplankton is usually represented by static (Redfield) ratios, entirely ignoring its highly variable nature (Klausmeier et al., 2008), which can affect model sensitivity to climate change (Kwiatkowski et al., 2018). The problem extends

40 also to the representation of fundamental biotic processes, such as nutrient uptake or zooplankton foraging. For example, Smith et al. (2009) showed that the half-saturation concentration of nitrate use varies systematically with nitrate concentration and suggested that optimal uptake kinetics (Pahlow, 2005) may be more appropriate than the commonly-used Michaelis-Menten kinetics for simulating phytoplankton nutrient uptake. Zooplankton foraging behaviour can be characterized by a significant feeding threshold followed by a steep increase in ingestion (e.g., Kiørboe et al., 1985; Strom, 1991; Gismervik,

45 2005), which has also been demonstrated for a natural plankton community in the Sargasso Sea (Lessard and Murrell, 1998). This kind of feeding behaviour may be important for capturing the distribution of primary production in large ocean areas (Strom et al., 2000), but it is not represented by the Holling type II and III models (Holling and Buckingham, 1976) used in current biogeochemical models.

We have recently developed optimality-based formulations for phytoplankton and zooplankton (Pahlow and Prowe, 2010;

50 Pahlow et al., 2013), which can describe observed plasticity of organism composition and function, including phytoplankton variable Chl:C:N:P stoichiometry, the ability to fix nitrogen, and zooplankton feeding thresholds, yet are sufficiently simple for implementation in global biogeochemical models. These formulations have shown their ability to describe ecosystem behaviour in 0D and 1D modelling studies (e.g., Fernández-Castro et al., 2016; Su et al., 2018), and to predict patterns of phytoplankton nutrient and light colimitation based on satellite and in situ observations (Arteaga et al., 2014). In this contribution, we

55 describe the implementation of our new optimality-based plankton-ecosystem model (OPEM) into a global 3D ocean model component of an ESM of intermediate complexity. The model employed is the University-of-Victoria Earth System Climate model (UVic in the following, Eby et al., 2009; Weaver et al., 2001). Owing to its coarse spatiotemporal resolution, UVic is

a practical choice when working on long time scales (e.g., Niemeyer et al., 2017) and/or when many simulations are needed. Computational efficiency is also one of the main impediments to introducing more mechanistic formulations of biotic pro-

60   cesses (Chen and Smith, 2018), as, e.g., the representation of variable C:N:P stoichiometry requires additional tracers, which must be mixed and advected as well. UVic has been used extensively with typical state-of-the-art fixed-stoichiometry NPZD (nutrients-phytoplankton-zooplankton-detritus)-type marine ecosystem and biogeochemistry models (e.g., Keller et al., 2012; Niemeyer et al., 2017; Oschlies et al., 2017). Here we compare the behaviour of the OPEM with that of a previous UVic con-figuration, described in Nickelsen et al. (2015), modified with several improvements and bug fixes as described below. Since

65   the calibration of the OPEM embedded in UVic presents a major challenge, it is dealt with in the companion paper (Chien et al., 2019).

2   Optimality-based plankton in the UVic model

The UVic model version 2.9 (Weaver et al., 2001; Eby et al., 2013) in the configuration of Nickelsen et al. (2015) with the isopycnal diffusivity modifications by Getzlaff and Dietze (2013), vertically increasing sinking velocity of detritus (Kriest,

70   2017), and several bug-fixes (some of which were already introduced by Kvale et al., 2017, see Appendix A for the new bug fixes applied here) is referred to as the original UVic in the following. We base our new configurations on this original UVic, except that we use constant half-saturation iron concentrations and omit the upper temperature limit in the zooplankton temperature dependence. For OPEM, we replace the formulations for phytoplankton, diazotrophs and zooplankton in the original UVic model with an optimality-based model (Pahlow et al., 2013) for phytoplankton and diazotrophs, and the optimal

75   current-feeding model (Pahlow and Prowe, 2010) for zooplankton (Fig. 1).

One of the main problems for implementing variable stoichiometry in UVic's finite-difference code is the occurrence of negative concentrations in UVic, predominantly owing to its semi-implicit vertical mixing scheme (with smaller contributions arising from advection, the explicit isopycnal mixing scheme, and high-latitude filtering), as revealed by detailed inspection of the model's behaviour. Inside its biogeochemical module, UVic deals with negative concentrations by preventing, at every time

80   step and in every grid box, any fluxes out of negative tracer compartments, although several bugs in the original code previously rendered this mechanism partly ineffective. UVic also applies a flux-corrected central-differencing scheme for tracer advection (flux-corrected transport, FCT, applied here also in the vertical) in order to prevent generation of negative concentrations. Negative concentrations are also generated in the main biogeochemical module of UVic (subroutine npzd_src), owing to the long time-steps (we use 0.5 times the physical time step of 30 h and, if this would generate negative tracer concentrations,

85   subcycle with 0.25 times the physical time step) and the Euler scheme used for calculating the sources-minus-sinks terms.

For many cases (parameter settings), phytoplankton and/or diazotrophs can end up negative everywhere, compromising our calibration procedure, which depends on the reliability of simultaneous evaluation of simulation ensembles (see Section 2.4 below and Chien et al., 2019). We have addressed the problem by limiting the biological tracer fluxes of the sub-cycled biological time step at every grid box, so that not more than 90 % of any tracer is removed within any grid box during one

90   time step. In order to counter the generation of negative concentrations by advection and vertical mixing, we also modify the

physical transport of all particulate tracers and dissolved iron as follows: The sources-minus-sinks terms of the biogeochemical module are applied before calculating advective and diffusive fluxes, so that diffusion is the only remaining source of negative concentrations. In all cases where the sum of all diffusive fluxes ($\mathcal{D}$) would remove more of a tracer than is present in a grid cell after applying advective fluxes ($\mathcal{T}$), we calculate a correction factor, $f_{\mathcal{D}} = -\mathcal{T}/(\mathcal{D} \times \Delta t)$, where Δt is the time step, which

95   is then multiplied with all outward diffusive fluxes to ensure a non-negative tracer concentration. Since limiting the flux out of one grid cell reduces the flux into the neighbouring cell, this procedure is applied recursively until non-negative concentrations are guaranteed everywhere. Whenever high-latitude filtering (Kvale et al., 2017) results in negative concentrations, we multiply positive changes $\Delta\mathcal{T}^+$ by a factor $f_{\text{filt}} = \sum_{\mathcal{T}_{\text{filt}} < 0.1\mathcal{T}} (0.1\mathcal{T} - \mathcal{T}_{\text{filt}}) / \sum \Delta\mathcal{T}^+$ and hence allow filtering-induced reductions by at most 90 %, where $\mathcal{T}_{\text{filt}}$ is the (possibly negative) result of the high-latitude filter.
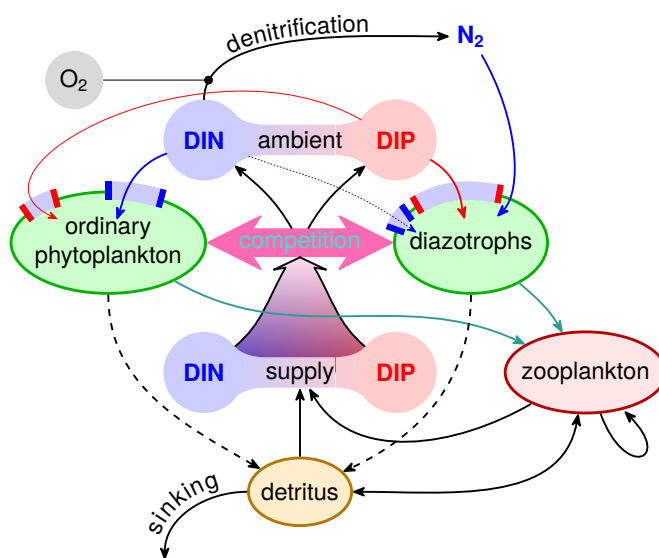

Figure 1. Optimality-based plankton-ecosystem model (OPEM). Ordinary phytoplankton, diazotrophs, and zooplankton are represented by optimality-based physiological regulatory formulations.

100   2.1   Phytoplankton and diazotrophs

Ordinary and diazotrophic phytoplankton are described by the optimal-growth model (OGM) of Pahlow et al. (2013), modified to account for the coarse spatio-temporal resolution of UVic and augmented with temperature and iron effects (see equations provided below). Owing to the relatively long time step, the model does not resolve the dynamics of photo-acclimation and we therefore describe the Chl:C ratio of the chloroplast by its balanced-growth optimum. Hence we do not need state variables for

105   Chl. Simulating variable Chl:C:N:P stoichiometry in phytoplankton then requires three state variables, representing particulate organic C, N, P (POC, PON, POP) for each phytoplankton group and for detritus.

The OGM is a cell-quota model comprising several levels of physiological regulation. At the whole-cell level, resources are optimally allocated between nutrient acquisition and CO_2 fixation, Chl synthesis is optimised within the chloroplast, and optimal uptake kinetics (Pahlow, 2005; Smith et al., 2009) drives nutrient uptake and assimilation inside the protoplast. For

110   all trade-offs, we define optimal as yielding maximum balanced growth of the cell. For facultative diazotrophs, N_2 fixation

is switched on whenever this enhances growth. The biological model parameters of the OGM are different from the original UVic configuration. In spite of its ability to describe two additional tracers (phytoplankton C and P) and the Chl:C ratio, the OGM has only 8 parameters (maximum rate V_0, nutrient affinity A_0, costs of N assimilation ζ^N and Chl synthesis ζ^{Chl} and maintenance R_M^{Chl}, subsistence quotas Q_0^N and Q_0^P, and the light-absorption coefficient α), i.e., the same as the phytoplankton parameters of the original UVic configuration (Nickelsen et al., 2015).

None of the measures against negative concentrations are effective if the minimum required concentration of a tracer is greater than zero, which is the case for our phytoplankton PON and POP tracers, whose minimum (subsistence) concentrations are given by the product of POC and the N and P subsistence quotas Q_0^N and Q_0^P, respectively, which can be thought of as the subsistence PON and POP of phytoplankton. In order to circumvent this problem and also be able to benefit from the FCT technique, we define δ-tracers as the differences between actual and subsistence phytoplankton PON and POP concentrations. The lower limit of the δ-tracers is 0, the δ-tracers can be transported with the positive transport schemes, and subsistence PON and POP are implicitly advected and mixed in proportion to phytoplankton POC and added back onto the δ-tracers where required:

$$\delta n_p = n_p - C_p \cdot Q_{0,p}^n \qquad \Leftrightarrow \qquad n_p = \delta n_p + C_p \cdot Q_{0,p}^n, \qquad n \in \{N, P\}, \qquad p \in \{phy, dia\} \tag{1}$$

where C_p, N_p, P_p are POC, PON, POP, respectively, of phytoplankton group p (phytoplankton or diazotrophs).

Table 1. Parameters and variables of the optimality-based plankton compartments.

Symbol(s)	Units	Description
DIN, DIP	$mol\,m^{-3}$	dissolved inorganic N, P
ϵ	m^{-1}	light-attenuation coefficient
T	$°C$	temperature
phytoplankton and diazotrophs		
A_0	$m^3\,(mol\,C)^{-1}\,d^{-1}$	potential nutrient affinity
α	$m^2\,W^{-1}\,mol\,C\,(g\,Chl)^{-1}\,d^{-1}$	potential light affinity
ζ^{Chl}	$mol\,C\,(g\,Chl)^{-1}$	cost of chlorophyll synthesis
ζ^N	$mol\,C\,(mol\,N)^{-1}$	cost of N assimilation
$\delta N, \delta P$	$mol\,m^{-3}$	$N - C \cdot Q_0^N, P - C \cdot Q_0^P$
F_0, F_0^N	$mol\,(mol\,C)^{-1}\,d^{-1}$	potential, temperature-dependent rate of N_2 fixation
f_C, f_F, f_V	—	allocation for CO_2 fixation, N_2 fixation, nutrient uptake
f_N	—	relative (to f_V) allocation for N uptake
$f(T)$	—	temperature dependence
k_{Fe}	$mmol\,m^{-3}$	half-saturation Fe concentration
L_{day}	—	day length
I, I_{min}	$W\,m^{-2}$	actual, minimum irradiance
λ, M	d^{-1}	leakage, mortality

Table 1. (continued)

Symbol(s)	Units	Description
μ	d^{-1}	net relative growth rate
Q^N, Q^P	$mol\,(mol\,C)^{-1}$	N:C, P:C ratios (N, P cell quotas)
Q_0^N, Q_0^P	$mol\,(mol\,C)^{-1}$	N, P subsistence quotas
R	d^{-1}	respiration
R^{Chl}, R_M^{Chl}	d^{-1}	total, maintenance cost of chlorophyll
r_{DIC}	d^{-1}	extra DIC release
S_{Fe}, S_I	—	degree of iron, light saturation
θ	$g\,Chl\,(mol\,C)^{-1}$	Chl:C ratio[*]
V_0	$mol\,(mol\,C)^{-1}\,d^{-1}$	potential-rate parameter
V^C	d^{-1}	rate of C fixation
V^N, V^P	$mol\,(mol\,C)^{-1}\,d^{-1}$	rates of N, P uptake[*]
V_0^C, V_0^N, V_0^P	$mol\,(mol\,C)^{-1}\,d^{-1}$	temperature-dep. pot. rates of C, N, P acquisition
zooplankton and detritus		
$\mathcal{A}_f, \mathcal{A}_t$	d^{-1}	foraging, total activity
β	—	digestion-efficiency coefficient
c_a, c_f	—	cost of assimilation, foraging
E_{max}, E_{zoo}	—	max., actual assimilation efficiency
$f_{det}(T), f_{zoo}(T)$	—	detritus, zooplankton temperature dependence
$G_{prey}^C, G_{prey}^N, G_{prey}^P$	$mol\,m^{-3}\,d^{-1}$	prey-specific rate of C, N, P ingestion
g_{max}, g_{zoo}	d^{-1}	reference, actual relative rate of total ingestion
M_{zoo}	$m^3\,(mol\,C)^{-1}\,d^{-1}$	zooplankton mortality
μ_{zoo}	d^{-1}	net relative growth rate
ν_{det}	d^{-1}	detritus reference decay rate
Π^C, Π^N, Π^P	$mol\,m^{-3}$	effective prey C, N, P concentration
ϕ_p	$m^3\,(mol\,C)^{-1}$	prey-capture coefficients, $p \in \{phy, dia, det, zoo\}$
Q_{zoo}^N, Q_{zoo}^P	$mol\,(mol\,C)^{-1}$	zooplankton N:C, P:C ratio
$R_{zoo}^C, X_{zoo}^N, X_{zoo}^P$	$mol\,m^{-3}\,d^{-1}$	respiration, dissolved N, P loss
r_Q	—	stoichiometric reduction factor
S_g	—	degree of ingestion saturation

[*]variants with hat (ˆ) accents are relative to the chloroplast or protoplast

The local rates of change of the phytoplankton tracers are then defined by sources-minus-sinks terms ($\mathcal{S}$):

$$\mathcal{S}(C_p) = (\mu_p - \lambda_p - M_p) \cdot C_p - G_p^C, \qquad\qquad p \in \{phy, dia\} \qquad (2)$$

$$\mathcal{S}(\delta n_p) = V_p^n \cdot C_p - (\lambda_p + M_p) \cdot n_p - G_p^n - \mathcal{S}(C_p) \cdot Q_{0,p}^n, \qquad n \in \{N, P\} \qquad (3)$$

where μ_p is net relative (C-specific) growth rate (C fixation minus the sum of respiration and release of dissolved organic

130   carbon by phytoplankton, immediately respired to DIC here), λ_p leakage, M_p mortality, G_p^n grazing by zooplankton, V_p^N and

V_p^P DIN and DIP uptake, and Q_p^N and Q_p^P biomass-normalised N and P cell quotas (N:C and P:C ratios). The last term in (3)

accounts for the subsistence amounts of N and P implicitly contained in C_p and subtracted from δn_p via (1). Leakage is the

fast-recycling term parametrising the microbial loop (Keller et al., 2012). Definitions for all terms in Eqs. (2) and (3) are

provided in Appendix B1.

135   We set up configurations with two representations of temperature dependence for diazotrophs, (1) configuration OPEM

with the same temperature dependence as in the original UVic, and (2) configuration OPEM-H with the same temperature

dependence (Eppley, 1972) applied to phy and dia growth and nutrient uptake, and the temperature function from Houlton

et al. (2008) for N_2 fixation (Fig. 2, see Appendix B1.3). All other temperature dependencies are unchanged from the original

UVic.

Figure 2. Temperature functions ($f_{\mathrm{dia}}(T)$) for N_2 fixation. The UVic function is the one employed by the original and OPEM configurations. The OPEM-H configuration applies the Eppley (1972) function to nutrient uptake and CO_2 fixation to both ordinary and diazotrophic phytoplankton and the Houlton et al. (2008) function to N_2 fixation.
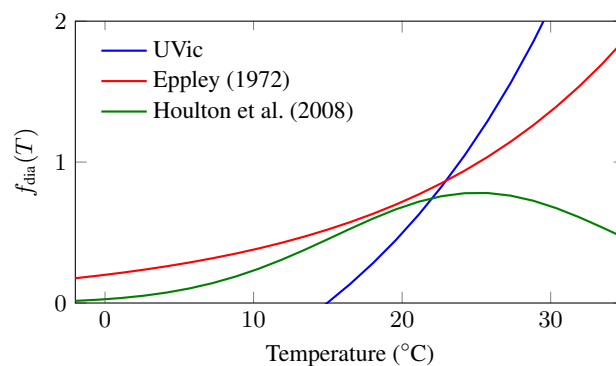
2.2 Zooplankton

Zooplankton foraging is described by the model of optimal current feeding (OCF, Pahlow and Prowe, 2010). The OCF is

based on the idea that the animal has a certain inherent maximum total activity ($\mathcal{A}_t$), which can be allocated between foraging

activity ($\mathcal{A}_f$) and activity for the assimilation of food ($\mathcal{A}_t - \mathcal{A}_f$), so that the net relative growth rate is maximised, considering

the costs of foraging and assimilation (represented by the coefficients c_f and c_a, respectively). While $\mathcal{A}_t$ is a rather abstract

145   quantity, it can be expressed as a function of the maximal ingestion rate, which is routinely determined in feeding experiments,

and temperature (see Eq. (B18) in Appendix B2). The OCF can represent different foraging strategies via its prey-capture

coefficient (ϕ) and c_f. Very low ϕ and $c_f \approx 0$ represent ambush feeding, whereas $c_f \approx c_a$ is representative of current feeding

for intermediate ϕ and cruise feeding for high ϕ. The parameter values in OPEM and OPEM-H (Table 2) are between values

determined for cruise and current feeders by Pahlow and Prowe (2010).

150   Besides its mechanistic foundation, the main advantages over the Holling-II formulation in the original UVic model are

the predicted feeding threshold and variable assimilation efficiency. Assimilation efficiency is constant and a feeding threshold

does not exist in the original UVic model. Temperature dependence is accounted for by multiplying the maximum ingestion rate

and maintenance respiration with the temperature function as described in Keller et al. (2012) but here without the cap at 20 °C. The cap on the increase of maximum ingestion rate with grazing in the original version was deemed necessary in order to avoid

155 inordinately high grazing in the tropics (Keller et al., 2012). It is noteworthy that this does not appear to be a problem in OPEM even though maximum ingestion rates g_max are about 4-fold higher than in the original UVic version (Table 2). We attribute this to the feeding threshold in the OCF, which reduces grazing in oligotrophic regions. Since zooplankton stoichiometry is fixed (constant $Q_\mathrm{zoo}^\mathrm{N}$ and $Q_\mathrm{zoo}^\mathrm{P}$) but that of the food is variable, any excess C, N, or P must be released, assumed here in mostly dissolved form (as inorganic nutrients). To this end we define a stoichiometric reduction factor r_Q that reduces net uptake and

160 growth of zooplankton to the uptake of the most limiting nutrient of the ingested food,

$$r_\mathrm{Q} = \min\left(\frac{\Pi^\mathrm{N}}{\Pi^\mathrm{C} \cdot Q_\mathrm{zoo}^\mathrm{N}}, \frac{\Pi^\mathrm{P}}{\Pi^\mathrm{C} \cdot Q_\mathrm{zoo}^\mathrm{P}}, 1\right), \qquad \Pi^n = \sum_{p \in \{\text{phy, dia, det, zoo}\}} \phi_p n_p, \qquad n \in \{\mathrm{C, N, P}\} \tag{4}$$

where Π^n is the effective prey concentration for nutrient element n and ϕ_p are the prey-specific capture coefficients. The relations among the ϕ_p effectively determine the (relative) food preferences. The sources-minus-sinks term for zooplankton biomass $\mathcal{S}(\mathrm{N_{zoo}})$ is expressed here in terms of nitrogen, which can easily be converted to P and C via the zooplankton's fixed

165 stoichiometry. $\mathcal{S}(\mathrm{N_{zoo}})$ is the difference between net growth (μ_zoo), which is corrected for r_Q (Appendix B2), and losses due to predation ($G_\mathrm{zoo}^\mathrm{N}$) and mortality ($M_\mathrm{zoo}$):

$$\mathcal{S}(\mathrm{N_{zoo}}) = \mu_\mathrm{zoo} \cdot \mathrm{N_{zoo}} - G_\mathrm{zoo}^\mathrm{N} - M_\mathrm{zoo}\frac{N_\mathrm{zoo}^2}{Q_\mathrm{zoo}^\mathrm{N}} \tag{5}$$

Equations for μ_zoo and $G_\mathrm{zoo}^\mathrm{N}$ are given in Appendix B2.

2.3 Detritus and dissolved pools

170 Mortality terms and egestion of faecal particles by zooplankton produce detritus, which is itself subject to grazing and temperature-dependent remineralisation. We consider separate C, N, and P tracers for detritus:

$$\mathcal{S}(n_\mathrm{det}) = M_\mathrm{phy} \cdot n_\mathrm{phy} + M_\mathrm{dia} \cdot n_\mathrm{dia} + M_\mathrm{zoo} \cdot \frac{n_\mathrm{zoo}^2}{Q_\mathrm{zoo}^n} + X_\mathrm{zoo}^n - G_\mathrm{det}^n - f_\mathrm{det}(T) \cdot \nu_\mathrm{det} \cdot n_\mathrm{det}, \qquad n \in \{\mathrm{C, N, P}\} \tag{6}$$

where ν_det is the detritus remineralization rate at $0\,°\mathrm{C}$. Hence, the export and remineralisation fluxes are also traced individually for C, N, and P. This applies also to alkalinity, where we assume a sulfur-to-carbon ratio of $0.023\,\mathrm{mol\,S\,mol\,C^{-1}}$ for organic C

175 (Matrai and Keller, 1994). For $\mathrm{O_2}$ consumption during remineralisation, we consider contributions from C and N separately. We assume $-\mathrm{O_2:N} = 2$ during nitrification and calculate the respiratory quotient for C based on an $\mathrm{O_2:C}$ ratio of $170{:}117 = 1.45\,\mathrm{mol\,O_2\,mol\,C^{-1}}$ (Anderson and Sarmiento, 1994), corrected for the contribution of nitrification, assuming an average $\mathrm{C:N} = 6.625\,\mathrm{mol\,C\,mol\,N^{-1}}$, as $1.45 - 2/6.625 = 1.15\,\mathrm{mol\,O_2\,mol\,C^{-1}}$. Eq. (6) does not include gains and losses from sinking detritus particles. Detritus sinking speed v_sink increases with depth according to

180 $$v_\mathrm{sink} = v_0 + a_\mathrm{v} \cdot z \tag{7}$$

where $v_0 = 6\,\mathrm{m\,d^{-1}}$ is the sinking velocity at the surface, z is depth and $a_\mathrm{v} = 0.06\,\mathrm{d^{-1}}$ the rate of increase in v_sink with depth (Kriest, 2017).

Dissolved inorganic C and nutrients are utilised by phytoplankton and released by phytoplankton leakage, zooplankton respiration and excretion and detritus remineralisation, as well as via rejection of surplus elements via grazing of organic matter with elemental stoichiometries differing from that of zooplankton.

2.4 Model reference simulations

Table 2. Parameter settings for the original and our reference OPEM and OPEM-H configurations. Parameters in **bold** vary within the ensembles of simulations (Chien et al., 2019). Symbol descriptions are given in Table 1.

Parameter	Original	OPEM/OPEM-H	
$\boldsymbol{A_{0,dia}}$	—	$0.75 \times A_{0,phy}$[a]	$\mathrm{m^3\,(mol\,C)^{-1}\,d^{-1}}$
$\boldsymbol{A_{0,phy}}$	—	229	$\mathrm{m^3\,(mol\,C)^{-1}\,d^{-1}}$
α_{dia}	0.13–0.53[b]	0.5[c]	$\mathrm{W\,m^{-2}\,mol\,C\,(g\,Chl)^{-1}\,d^{-1}}$
α_{phy}	0.13–0.53[b]	0.4[c]	$\mathrm{W\,m^{-2}\,mol\,C\,(g\,Chl)^{-1}\,d^{-1}}$
β	—	0.2	
$c_a = c_f$	—	0.1	
E_{max}	—	1	
$\boldsymbol{g_{max}}$	0.4	1.75	$\mathrm{d^{-1}}$
$\boldsymbol{k_{Fe,dia}}$	0.10×10^{-3}	$2 \times k_{Fe,phy}$[d]	$\mathrm{mmol\,m^{-3}}$
$\boldsymbol{k_{Fe,phy}}$	0.12×10^{-3}	0.066×10^{-3}	$\mathrm{mmol\,m^{-3}}$
$\boldsymbol{\lambda_{0,phy} = M_{0,dia}}$	0.015	0.018	$\mathrm{d^{-1}}$
$\lambda_{0,dia}$	0	0	$\mathrm{d^{-1}}$
$M_{0,phy}$	0.03	0.03	$\mathrm{d^{-1}}$
$\boldsymbol{\nu_{det}}$	0.07	0.087	$\mathrm{d^{-1}}$
$\boldsymbol{\phi_{dia}}$	—	232	$\mathrm{m^3\,(mol\,C)^{-1}}$
$\boldsymbol{\phi_{phy}}$	—	118	$\mathrm{m^3\,(mol\,C)^{-1}}$
$\boldsymbol{\phi_{det}}$	—	94	$\mathrm{m^3\,(mol\,C)^{-1}}$
$\boldsymbol{\phi_{zoo}}$	—	118	$\mathrm{m^3\,(mol\,C)^{-1}}$
$\boldsymbol{Q^N_{0,dia}}$	—	0.067	$\mathrm{mol\,(mol\,C)^{-1}}$
$\boldsymbol{Q^N_{0,phy}}$	—	0.041 28	$\mathrm{mol\,(mol\,C)^{-1}}$
$\boldsymbol{Q^P_{0,dia}}$	—	0.002 71	$\mathrm{mol\,(mol\,C)^{-1}}$
$\boldsymbol{Q^P_{0,phy}}$	—	0.0022	$\mathrm{mol\,(mol\,C)^{-1}}$

[a] $A_{0,dia} < A_{0,phy}$ according to Pahlow et al. (2013)

[b] minimum and maximum, see Nickelsen et al. (2015)

[c] $\alpha_{dia} > \alpha_{phy}$ according to Pahlow et al. (2013)

[d] the higher $k_{Fe,dia}$ represents the larger Fe requirement of diazotrophs

We first did a preliminary sensitivity analysis to identify sensitive model parameters. Then we set up an ensemble of 400 parameter sets and ran both of our model configurations into steady state for all parameter sets. We select two reference simulations, one each from the OPEM and OPEM-H ensembles, according to a cost function and the ability to predict realistic

190 levels of water-column denitrification (Chien et al., 2019). The cost function quantifies the model-data misfit by a measure of the discrepancies between observed and simulated O_2, NO_3^-, PO_4^{3-}, and Chl, considering also correlations and covariances (Chien et al., 2019).

In the following we describe and discuss the behaviour of the two reference simulations, which turned out to have same parameter set (Table 2). While this may be a coincidence, it has the advantage that all differences between OPEM and OPEM-

195 H can be ascribed unequivocally to the difference in the temperature dependence of the diazotrophs. We specifically consider the models' ability to reproduce features not included in the cost function, namely the excess nitrate with respect to phosphate, termed $N^* = NO_3^- - 16 \cdot PO_4^{3-} + 2.9 \, \mathrm{mmol \, m^{-3}}$ (Gruber and Sarmiento, 1997; Mills et al., 2015), and global N_2-fixation rates and distributions within current observational ranges. All our UVic-model results are shown as annual averages at the end of the spin-up (i.e. after at least 10,000 years), when a seasonally cycling steady state has been reached.
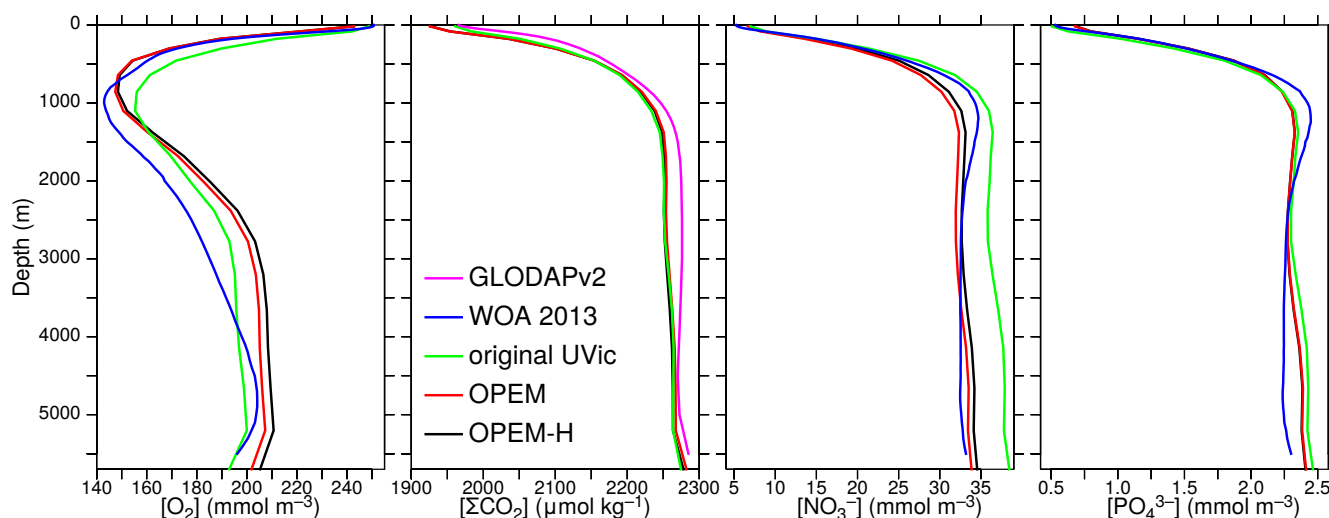

Figure 3. Globally-averaged vertical profiles of O_2, DIC (ΣCO_2), NO_3^-, and PO_4^{3-} concentrations. Oxygen, nitrate, phosphate, but not DIC are considered in the cost function. O_2, NO_3^-, and PO_4^{3-} data from the World Ocean Atlas 2013 (WOA 2013, Garcia et al., 2013a, b) and ΣCO_2 data from GLODAPv2 (Key et al., 2015; Lauvset et al., 2016) are compared to our original, OPEM, and OPEM-H UVic configurations (Section 2.4). Note that the PO_4^{3-} profiles coincide for OPEM and OPEM-H.

200 We compare the predictions of our reference simulations with data from these sources: NO_3^-, PO_4^{3-}, and O_2 data are from the World Ocean Atlas 2013 annual objectively analysed mean fields (WOA 2013, Garcia et al., 2013a, b). Dissolved inorganic C (DIC) data are from GLODAPv2 (Key et al., 2015; Lauvset et al., 2016). Estimates of Chl (MODIS Aqua, level 3,

https://oceancolor.gsfc.nasa.gov/l3, Hu et al., 2012), net primary and community production (NPP and NCP, Westberry et al., 2008; Li and Cassar, 2016) are based on satellite data. In situ N_2 fixation data are from MAREDAT (Luo et al., 2012).
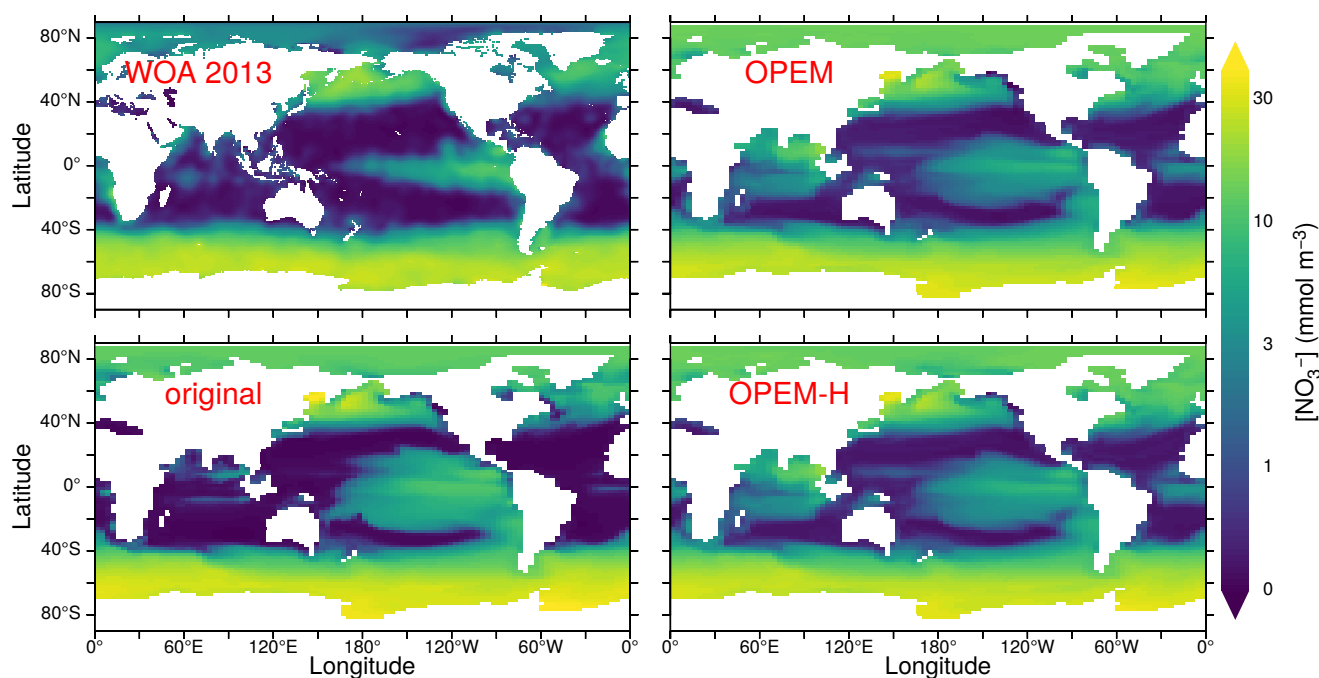
205 3   Model behaviour

Figure 4. Annually-averaged distribution of NO_3^- in the upper 50 m in the WOA 2013 climatology, and predicted from the original, OPEM, and OPEM-H UVic simulations.

3.1   Vertical and horizontal nutrient distributions

Horizontally-averaged vertical profiles of O_2 in the OPEM and OPEM-H simulations are closer to the WOA 2013 data in the upper 1500 m than in the original UVic model. At intermediate depths, all model versions overestimate O_2 concentrations, OPEM and OPEM-H slightly more so than the original UVic (Fig. 3). The original UVic better reproduces the NO_3^- pro-
210   file above 1000 m than OPEM and OPEM-H but overestimates NO_3^- below 2000 m. The DIC and PO_4^{3-} profiles from our reference simulations are very similar to those of the original UVic model (Fig. 3).

Surface nitrate concentrations are generally slightly higher and more evenly distributed in OPEM and OPEM-H than in the original UVic model (Fig. 4). For most of the Atlantic, OPEM and OPEM-H are closer to the WOA 2013 data. Surface NO_3^- in the Indian Ocean are underestimated by the original UVic and overestimated by OPEM and OPEM-H. Surface patterns of
215   N* are much closer to observations in both OPEM and OPEM-H than in the original UVic configuration (Fig. 5). However,

11

while N* in the northern North Pacific and Arctic Oceans is lower in OPEM and OPEM-H than in the original UVic, all UVic configurations still fail to reproduce the very low N* in large parts of the North Pacific and Arctic Oceans (Fig. 5). While N_2 fixation is not limited to temperatures higher than 15 °C in OPEM-H, only very little N_2 fixation occurs in the high northern and southern latitudes and thus cannot explain the higher surface N* values in OPEM-H there (see Section 3.3 below). In our

220 model simulations, low N* in the eastern tropical Pacific and South Atlantic result from denitrification in underlying oxygen-minimum zones (OMZs) (Landolfi et al., 2013). The original UVic configuration also displays very low N* in the Andaman Sea, whereas results of OPEM and OPEM-H are somewhat closer to the WOA 2013 data in the northern Indian Ocean (Fig. 5).
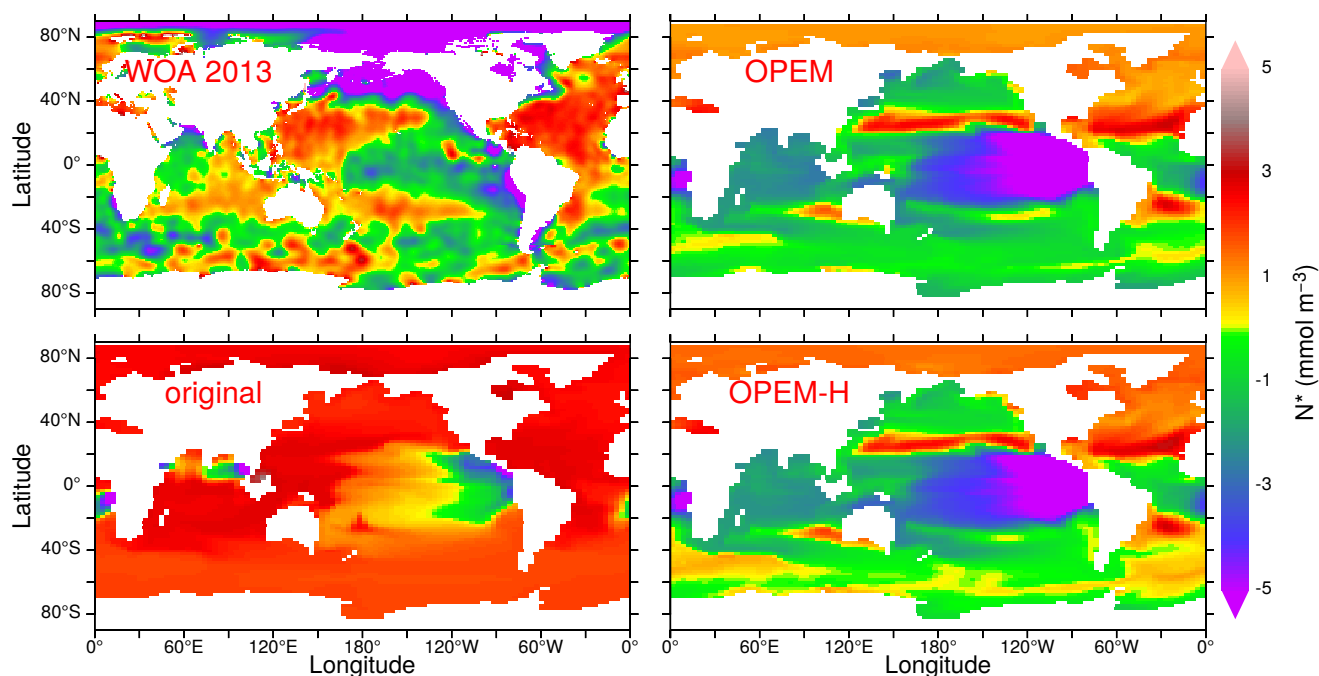

Figure 5. Annually-averaged distribution of N* in the upper 50 m in the WOA 2013 climatology and in the original, OPEM, and OPEM-H UVic simulations. Global averages for the upper 50 m are −0.4 mmol m^{-3} for the WOA 2013 and 1.8, −1.3, and −1.1 mmol m^{-3} for the original, OPEM, and OPEM-H simulations, respectively.

Interestingly, these differences cannot be seen in the O_2 distribution at 300 m, the depth of the OMZs, which is very similar in the Indian Ocean and eastern tropical Pacific among all our UVic simulations (Fig. 6), indicating that the carbon export and

225 subsequent remineralization is very similar as well. The main differences in O_2 distribution are that O_2 is slightly higher in the Arctic Ocean and slightly lower in the equatorial Pacific and northern North Pacific in both OPEM and OPEM-H compared to the original version (Fig. 6).

The OPEM simulations allow for a variable C:N ratio in detritus leaving the surface layers and reveal C:N ratios higher than the canonical value of 6.625 mol C (mol N)$^{-1}$, which is also the stoichiometry of zooplankton, almost everywhere between 40°S

230 and 40°N in OPEM and OPEM-H (Fig. 7). Thus, even though detritus C:N is lower in the Bay of Bengal than in the remainder
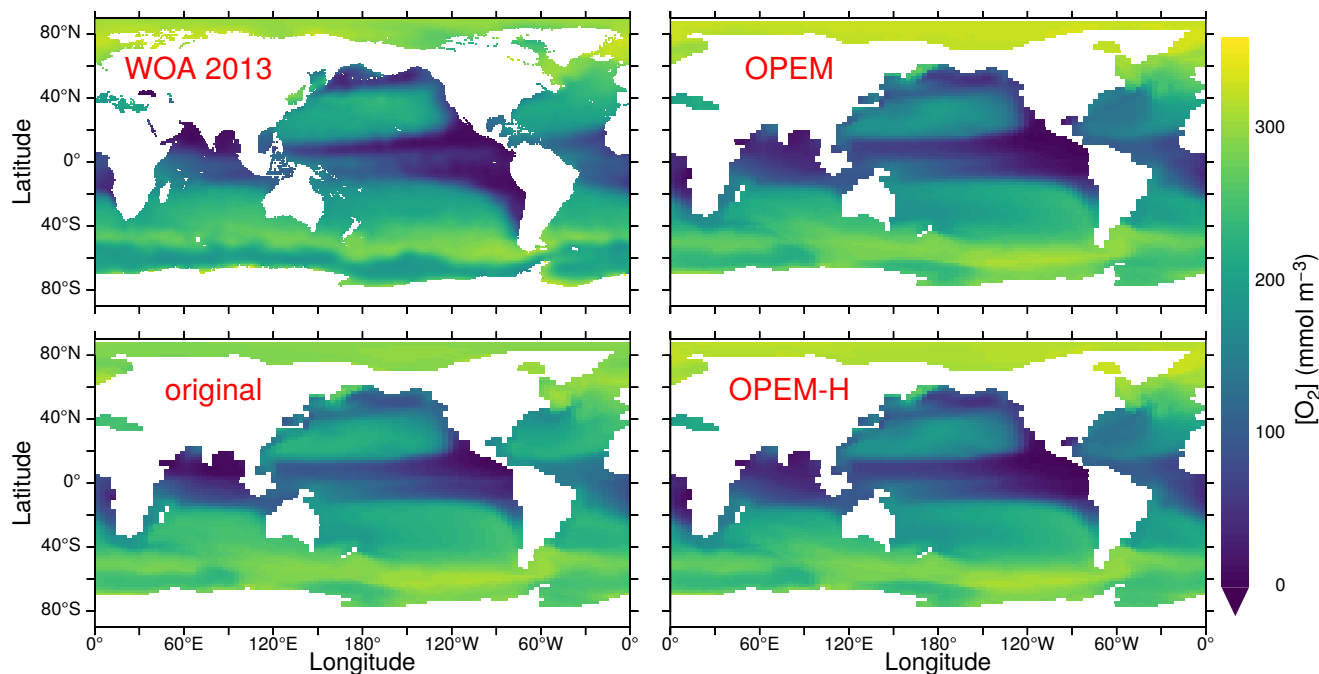
Figure 6. Annually-averaged distribution of O$_2$ concentration at 300 m in the WOA 2013 climatology and in the original, OPEM, and OPEM-H UVic simulations.

of the Indian Ocean in both OPEM simulations, this feature cannot explain the lower denitrification compared to the original UVic in this area, since the C:N ratio remains above the original UVic value of 6.625 mol C (mol N)$^{-1}$ and determines the O$_2$ demand for the remineralisation of sinking detritus.

Another interesting feature of the OPEM and OPEM-H simulations is their ability to reproduce, at least qualitatively, the
235   gradient of DIN:DIP ratios in the deep ocean (Fig. 8). The WOA 2013 data indicate relatively high DIN:DIP in the deep North Atlantic, decreasing towards the Southern, Indian, and Pacific Oceans. This gradient is very weak (and reversed) in the original UVic model (Fig. 8). Also, not all simulations in our OPEM and OPEM-H ensembles can reproduce this gradient. Thus, reproducing the deep DIN:DIP distribution appears to require the combination of decoupled C, N, and P with a suitable parameter set. Note that deep-water N:P ratios are systematically higher in OPEM-H compared to OPEM, because of the
240   elevated N* values in OPEM-H in high-latitude surface waters that feed the deep ocean interior (Fig. 5).

3.2 Chlorophyll and primary production

Chlorophyll concentrations are generally more evenly distributed in OPEM and OPEM-H, which agrees better with the MODIS Aqua (level 3) satellite estimates (Hu et al., 2012) than the original UVic model, which also overestimates chlorophyll in the tropics and the Indian Ocean more pronouncedly. Only the OPEM-H simulation predicts reasonably high chlorophyll in the
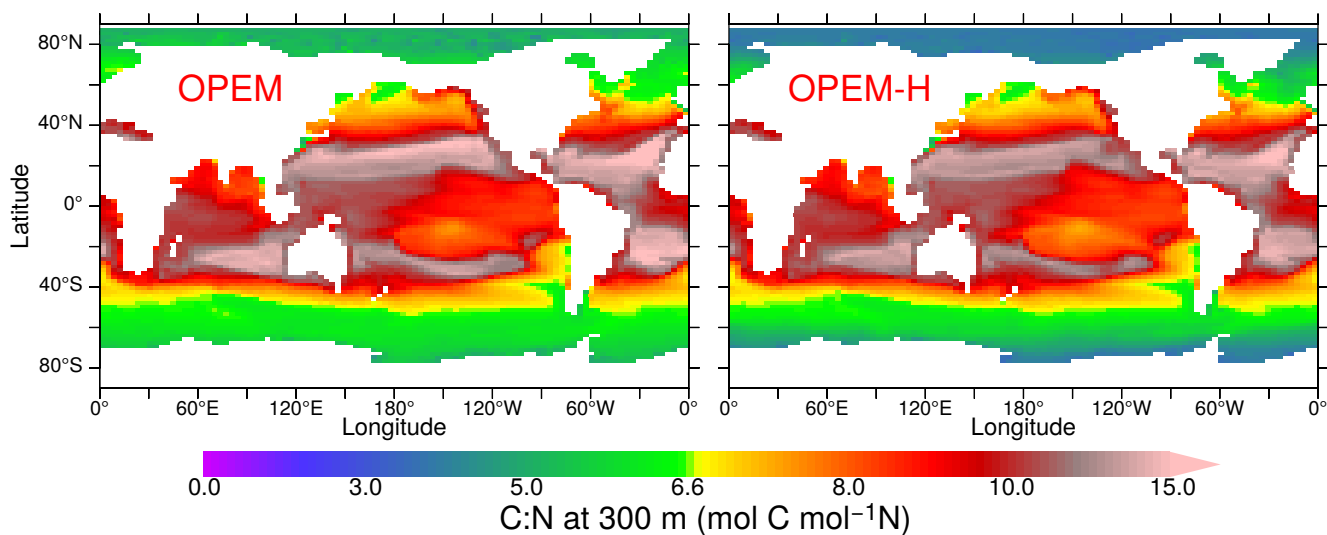245   Arctic Ocean compared to the satellite estimates (Fig. 9).

Geoscientific
Model Development
Discussions

Figure 7. Annually-averaged C:N ratio of detritus at 300 m in the OPEM and OPEM-H simulations. The colour bar is centered at 6.625 mol C (mol N)$^{-1}$, which is the C:N ratio of zooplankton in all our UVic simulations.
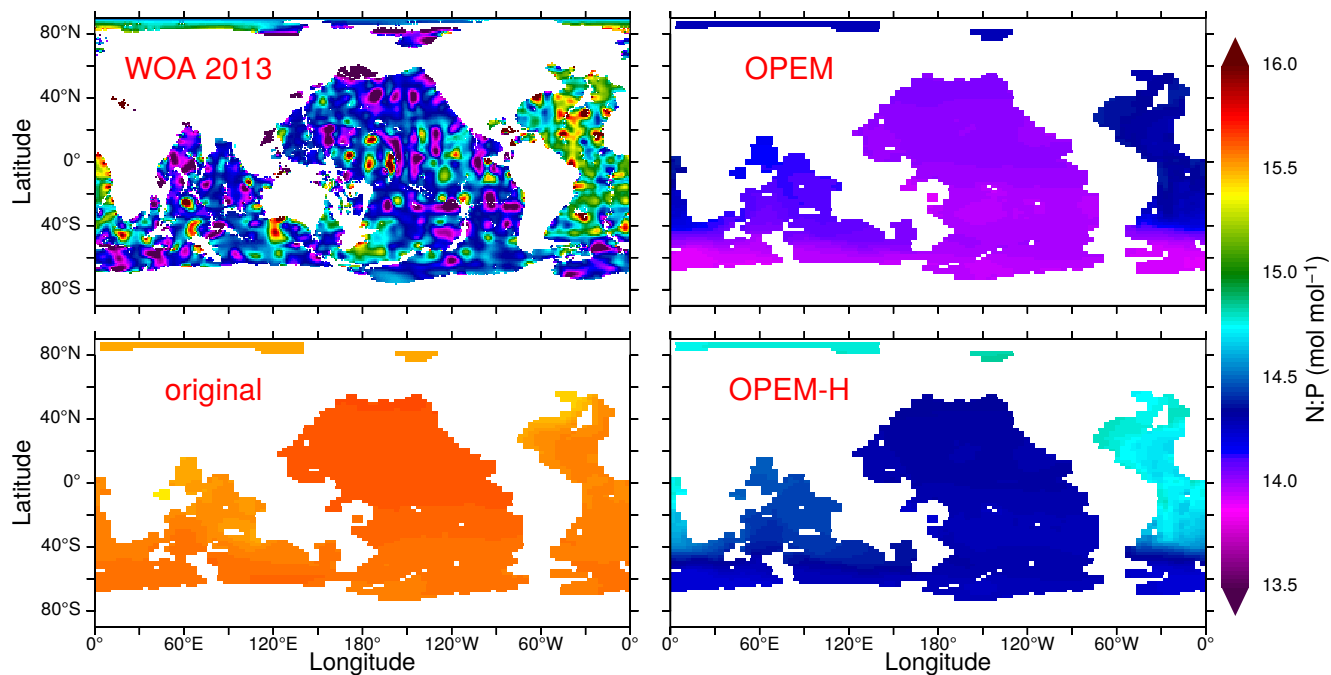

Figure 8. Distribution of DIN:DIP in the deep ocean (at 3200 m) in the WOA 2013 climatology and in the original, OPEM, and OPEM-H UVic simulations.
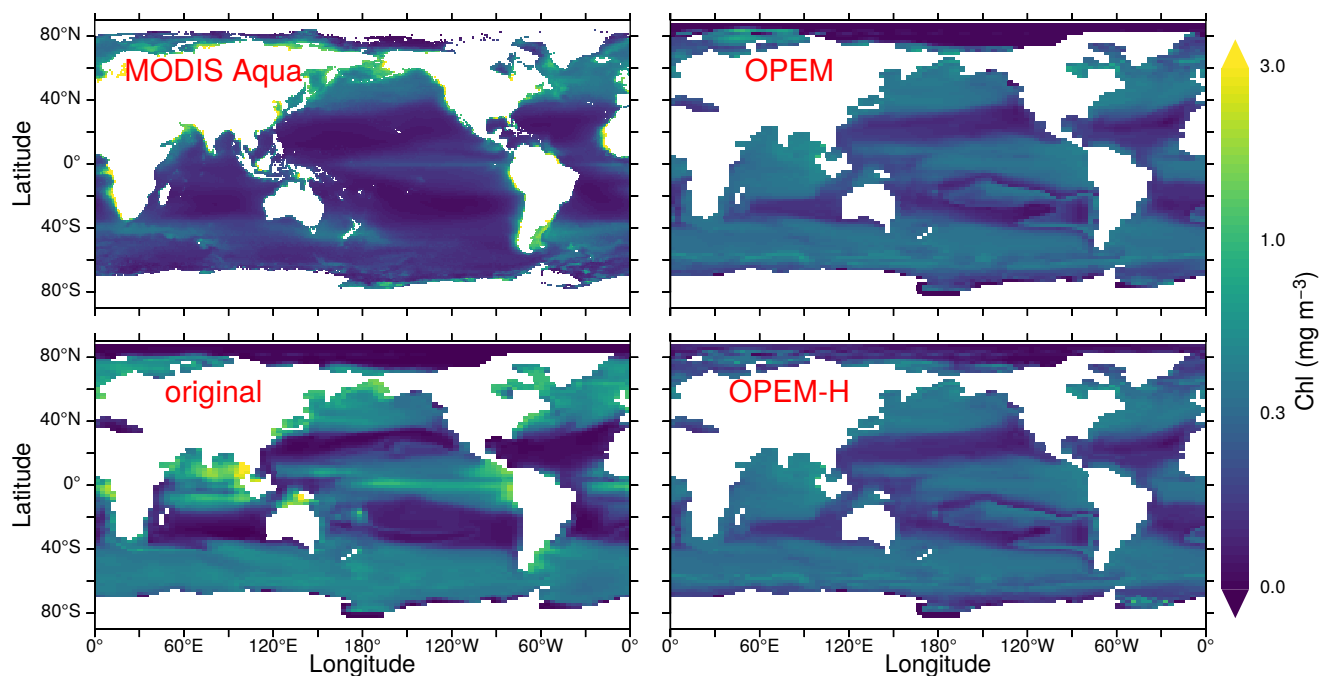
14

Figure 9. Annually averaged distribution of surface Chl estimated from MODIS Aqua (level 3) data for 2002 – 2019, and predicted from the original, OPEM, and OPEM-H UVic simulations. The MODIS Aqua averages in the top-left panel treat missing data as 0. Chl is calculated assuming Chl:N = 1.59 g mol^{-1} (Oschlies et al., 2000) for the original UVic model. Note that the surface layer is 50 m thick in UVic, whereas the satellite estimate is for the upper ~20 m.

Global net primary production is defined here as

$$\text{NPP} = (\mu_{\text{phy}} - \lambda_{\text{phy}}) \cdot C_{\text{phy}} + (\mu_{\text{dia}} - \lambda_{\text{dia}}) \cdot C_{\text{dia}} \qquad (8)$$

NPP in OPEM is the same as in OPEM-H (88.0 Pg C yr^{-1}) and is much higher than the estimate from Westberry et al. (2008) of 52 Pg C yr^{-1}, which in turn exceeds that in the original UVic model (44.3 Pg C yr^{-1}). The NPP for the original UVic is lower than previously published (55 Pg C yr^{-1}, Nickelsen et al., 2015) because we include λ_{phy} in Eq. (8). The global averages predicted by the OPEM and OPEM-H simulations are slightly higher than the range of predictions from ocean color- and model-based estimates reported by Carr et al. (2006). NPP is much more evenly distributed in OPEM and OPEM-H than in the original UVic model, but the carbon-based productivity model (CbPM) (Westberry et al., 2008) predicts an even more uniform distribution (Fig. 10). The original configuration clearly underestimates NPP in the oligotrophic gyres, whereas OPEM and OPEM-H overestimate NPP in the tropical ocean.

Another possible explanation for the discrepancy between the OPEM and CbPM predictions may be that we do not include light affinity (α) among the list of parameters to be calibrated, because this parameter showed relatively little effect during our preliminary sensitivity analysis used to select sensitive model parameters. However, Arteaga et al. (2016) found that simple adaptive equations for α and A_0, meant to represent adaptation to nutrient or light limitation, greatly improved predicted Chl:C

260 compared to constant α and A_0 as applied in the present study. The use of constant parameters means that the OPEM and OPEM-H represent physiological flexibility as observed within species, but do not consider variations in plankton community composition.
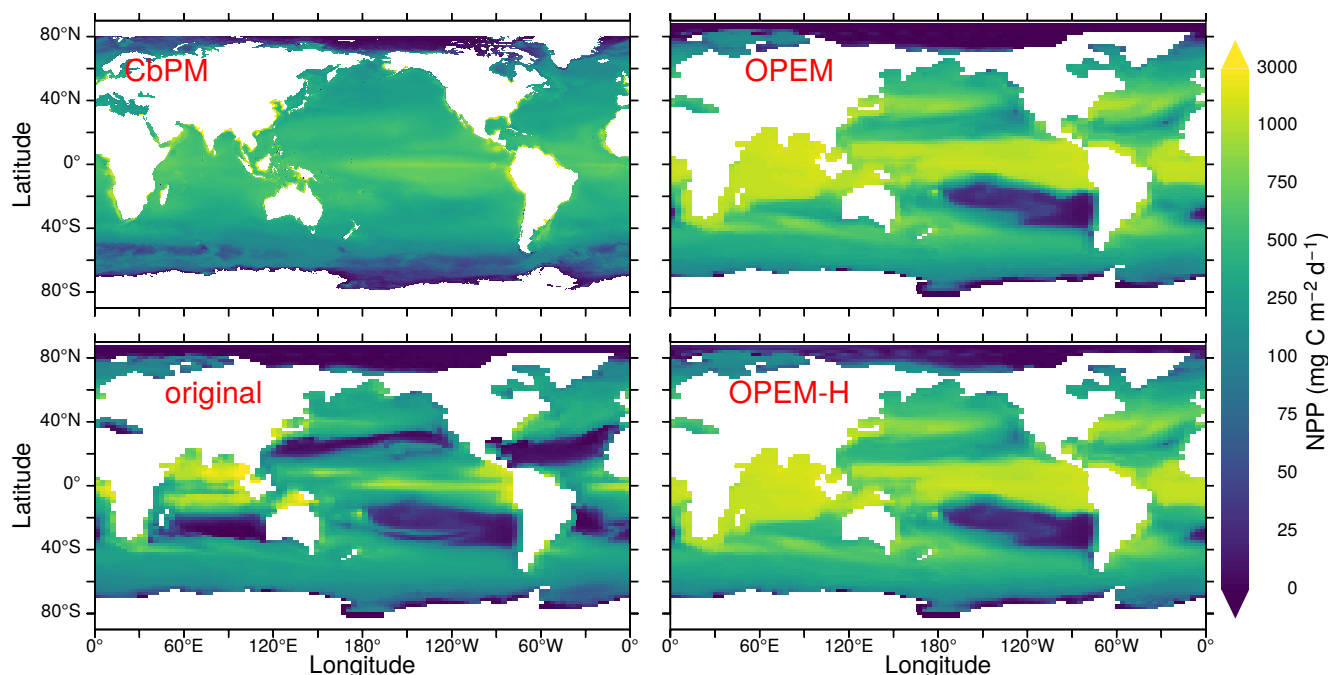

Figure 10. Annually-averaged distribution of vertically-integrated net primary production (NPP) estimated from satellite data via the C-based productivity model (CbPM) and predicted from the original, OPEM, and OPEM-H UVic simulations. The satellite-based CbPM estimate is the average for 2012–1018 (Westberry et al., 2008) with missing data treated as 0.

Net community production (NCP) is spatially more evenly distributed in OPEM and OPEM-H than in the original UVic model. Both the more evenly distribution and the subsequently higher global total NCP are much closer to the satellite-based

265 estimate of Li and Cassar (2016) than the original UVic model, except in the Indian Ocean (Fig. 11). The relatively low NPP in the original UVic model appears to be connected to a correspondingly low NCP ($9.3 \, \text{Pg C yr}^{-1}$), which is close to previous model predictions (clustering around $10 \, \text{Pg C yr}^{-1}$, Laws et al., 2000; Dunne et al., 2005; DeVries and Weber, 2017). The high (overestimated) NPP in OPEM and OPEM-H is associated with much higher NCP predictions (12.9 and $13.0 \, \text{Pg C yr}^{-1}$, respectively), which are much closer to the satellite-based estimate of $13.5 \, \text{Pg C yr}^{-1}$ (Fig. 11) based on Li and Cassar (2016).

270 ### 3.3 N_2 fixation and diazotrophs

N_2 fixation rates are shown in Fig. 12. Unfortunately, our model simulations differ most strongly in the Indian Ocean, for which no data exist in the MAREDAT database of Luo et al. (2012). One of the problems we face regarding N_2 fixation is that our UVic simulations do not include benthic denitrification and hence miss the dominant oceanic fixed-N loss term (e.g.,
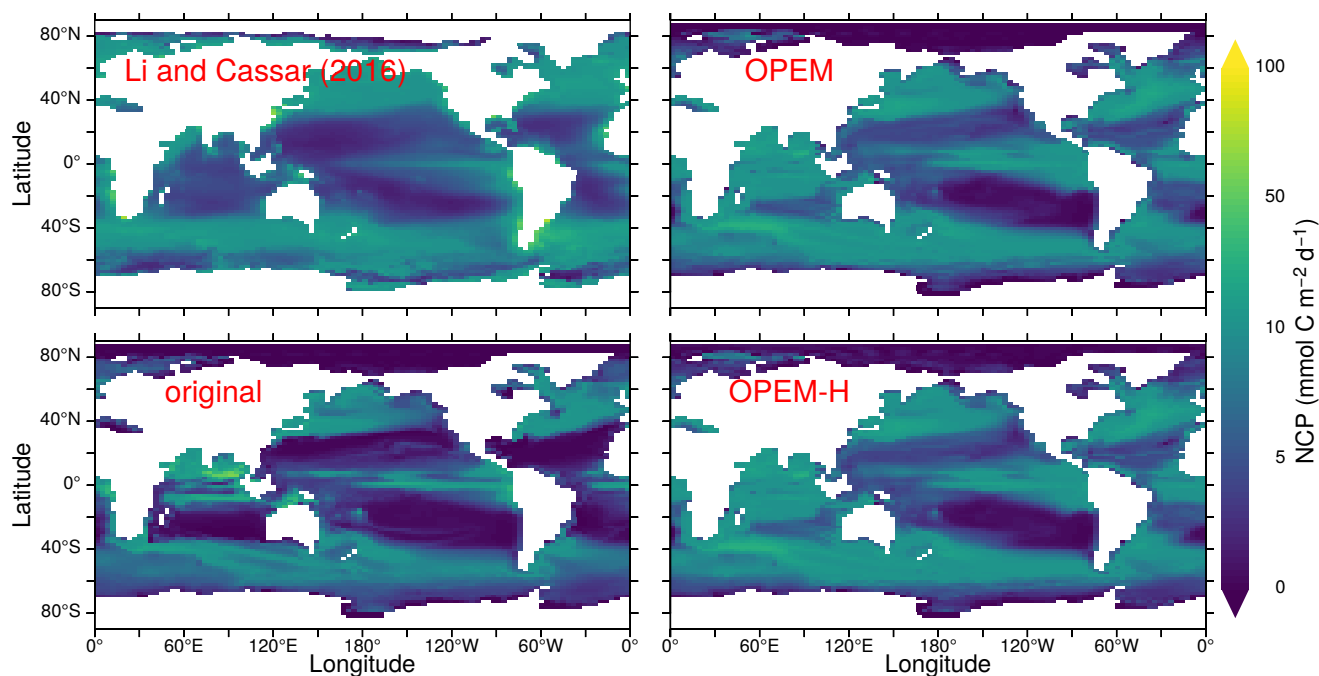
Geoscientific
Model Development
Discussions

Figure 11. Annually-averaged distribution of net community production (NCP) in the upper 100 m. Global oceanic NCP is 13.5 Pg C yr^{-1} for the satellite-based estimate from Li and Cassar (2016) and 9.3, 12.9, and 13.0 Pg C yr^{-1} for the original, OPEM, and OPEM-H simulations, respectively. The data from Li and Cassar (2016) are 1997–2010 averages of their genetic-programming results for SeaWiFS, aggregated into a monthly climatology on the UVic grid and then temporally averaged with missing data treated as 0.

Gruber, 2004; Wang et al., 2019). Since we have run the models into steady state, N$_2$ fixation must balance denitrification, which in our case occurs only in the water-column. Thus, our UVic simulations cannot be expected to generate realistic global rates of N$_2$ fixation unless water-column denitrification is strongly overestimated. Accordingly, our predicted N$_2$ fixation rates (53.9 Tg N yr^{-1} in the original UVic, 71.2 Tg N yr^{-1} in OPEM, and 69.4 Tg N yr^{-1} in OPEM-H, Fig. 12) are much closer to current estimates of water-column denitrification than total N$_2$ fixation ($\approx$ 70 vs. $\approx$ 160 Tg N yr^{-1}, Wang et al., 2019). Another major difference is the much larger relative contribution of northern-hemisphere N$_2$ fixation in OPEM and OPEM-H compared to the original UVic. The North Atlantic contributes only 4 % in the original UVic, but the 23 % and 24 % contributions in OPEM and OPEM-H, respectively, are closer to the observation-based estimate of 23 % reported by Landolfi et al. (2018), for the data from Luo et al. (2012), than any other model mentioned there.

Both OPEM and OPEM-H predict less N$_2$ fixation than the original UVic model in the Indian Ocean, which explains (at least partly) the differences in N* there (Fig. 5). OPEM and OPEM-H have no N$_2$ fixation in the northern Indian Ocean, which is an area of intense diazotrophy in the original UVic, owing the presence of diazotrophs in the original UVic and their absence in OPEM and OPEM-H in this region (Fig. 14). Other models, for example the one of Monteiro et al. (2011) also produce high rates of N$_2$ fixation in the northern Indian Ocean, similar to the distribution simulated by the original UVic. In contrast,
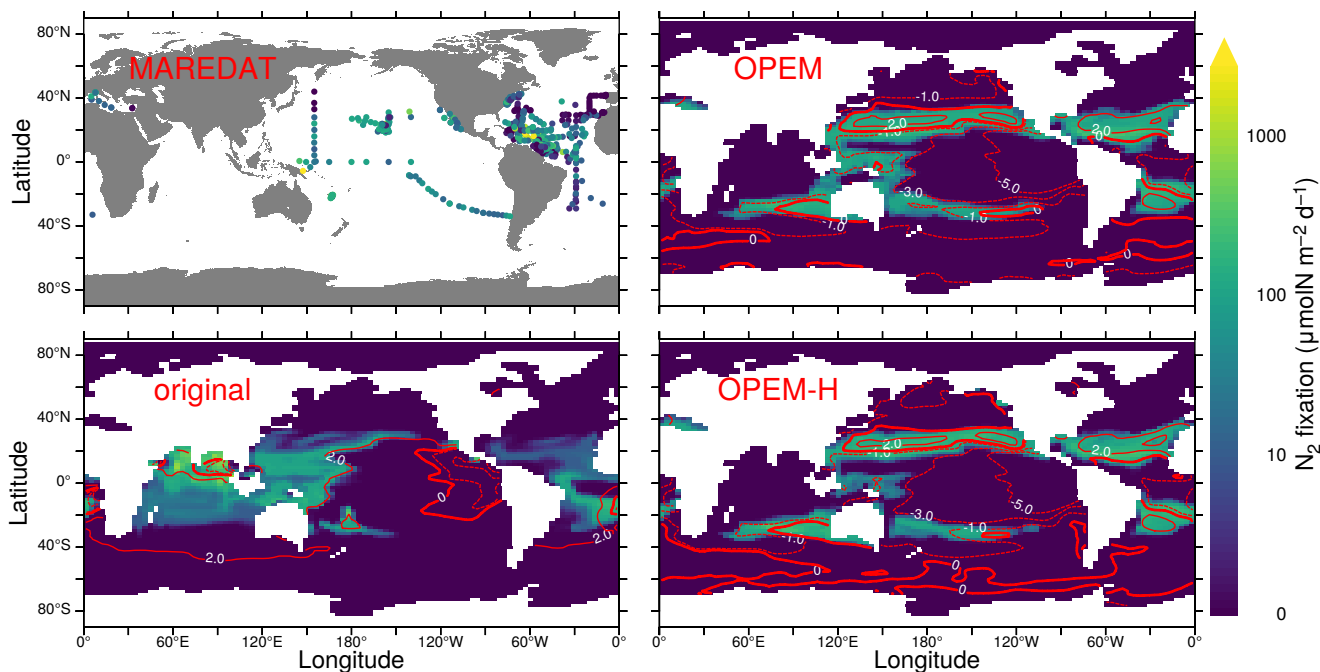
Figure 12. Annually-averaged and vertically-integrated rate of N_2 fixation in MAREDAT and the original UVic, OPEM, and OPEM-H simulations. Global oceanic N_2 fixation is 53.9, 71.2, and 69.4 Tg N yr^{-1} for the original UVic, OPEM and OPEM-H, respectively. Overlaid red contours indicate surface N*. The MAREDAT data are total N_2-fixation rates from Luo et al. (2012).

Löscher et al. (2019) recently found no evidence for significant N_2 fixation in the Bay of Bengal. Whether the qualitative change towards very little N_2 fixation also in other parts of the Indian Ocean, as simulated by both OPEM and OPEM-H, is a

290 qualitative improvement in the representation of N_2 fixation by biogeochemical ocean models, remains to be seen. OPEM-H predicts a wider geographical range for N_2 fixation than the other UVic configurations, owing to Houlton's 2008 temperature function for diazotrophy, now occurring in a few spots north of 40°N (Fig. 12). Mulholland et al. (2019) recently reported high rates for the east coast of North America. Thus, widening the temperature range of N_2 fixation as in OPEM-H could well be a prerequisite for a more realistic representation of diazotrophy.

295 Comparing the distributions of simulated N* and N_2 fixation reveals a positive relation with N_2 fixation, which occurs mostly in regions with N* > 0 (Fig. 12). This pattern is very different from that in the analysis of Deutsch et al. (2007), who assumed a high PO_4^{3-} demand of diazotrophs, whereas our model does not make this assumption and actually predicts that N_2 fixation can greatly increase the competitive ability of diazotrophs at low PO_4^{3-} concentrations (Pahlow et al., 2013). Thus, in our models the rise in N* due to N_2 fixation does not destroy the niche of the diazotrophs but rather creates an environment in

300 which their ability to utilise very low PO_4^{3-} concentrations allows them to persist. This ability derives from the absence of N limitation in the original UVic, and from the additional N allocation towards P uptake in OPEM and OPEM-H.
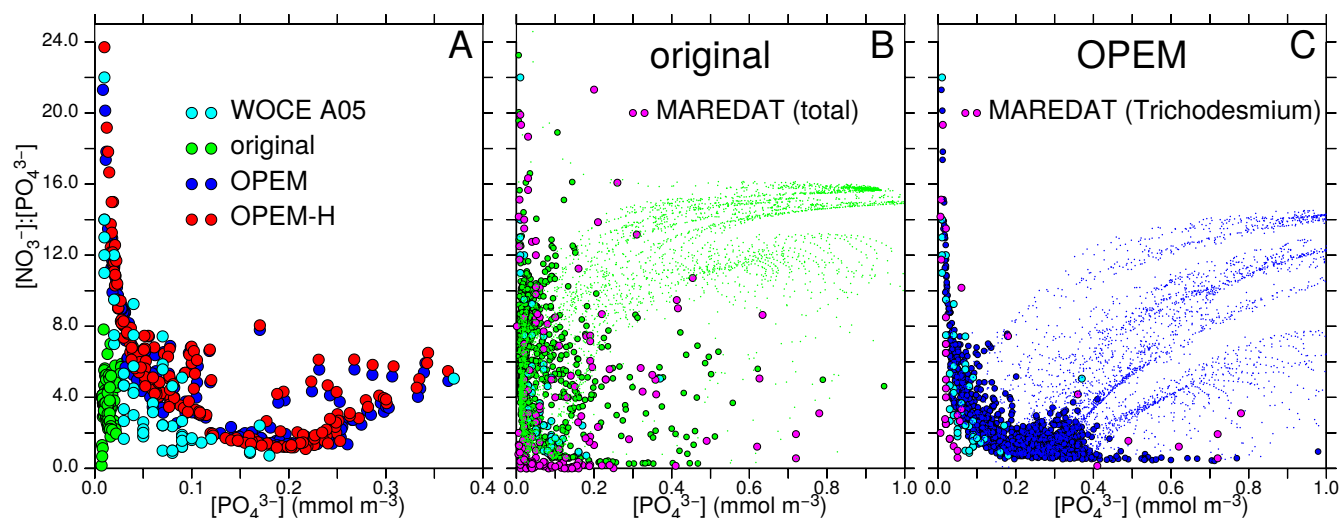
18

Figure 13. Patterns of surface NO_3^-/PO_4^{3-} vs. PO_4^{3-}. A Data from WOCE section A05 (Millero et al., 2000, along 24.5°N across the North Atlantic,) and results for 10°N–30°N in the North Atlantic from the original, OPEM and OPEM-H configurations. B and C Global patterns for the surface layer where $PO_4^{3-} \leq 1\,\mathrm{mmol\,m^{-3}}$ (dots), with green and blue disks highlighting results where N_2 fixation occurs in the original and OPEM simulations, respectively. The light-blue disks in B and C are the WOCE data from panel A. MAREDAT data are for locations with positive total (panel B) and *Trichodesmium* (panel C) N_2 fixation rates from Luo et al. (2012).

The high competitive ability of diazotrophs can be visualised in the pattern of NO_3^-/PO_4^{3-} vs. $[PO_4^{3-}]$, where N_2 fixation can occur under high NO_3^-/PO_4^{3-} ration only when $[PO_4^{3-}]$ is low in OPEM and OPEM-H (Fig. 13). Accordingly, Pahlow et al. (2013) suggested that the coexistence of ordinary and diazotrophic phytoplankton should result in a roughly

305   inverse relation between NO_3^-/PO_4^{3-} and $[PO_4^{3-}]$, which is indeed exhibited by data from WOCE section A05 in the subtropical North Atlantic (Millero et al., 2000). The pattern of NO_3^-/PO_4^{3-} vs. $[PO_4^{3-}]$ in OPEM and OPEM-H in this region approximately matches that in WOCE section A05, whereas the pattern is very different in the original UVic (Fig. 13A). The patterns for the global surface ocean reveal a similar inverse relation for the original UVic, albeit much less constrained than for OPEM (Fig. 13B, C). In both cases, the patterns for locations with N_2 fixation are very different from those for all

310   regions (green and blue dots in Fig. 13B, C). Whereas the pattern for the original UVic appears more similar to the pattern in the data from Luo et al. (2012) corresponding to total N_2 fixation, except where both NO_3^- and PO_4^{3-} are very low (Fig. 13B), the pattern in OPEM is closer to that where N_2 fixation by *Trichodesmium* occurs (Fig. 13C). While none of our UVic configurations can explain N_2 fixation occurring at very low NO_3^- and PO_4^{3-} concentrations (Fig. 13B), the physiology of N_2 fixation clearly has a strong influence on NO_3^-/PO_4^{3-} and hence N* patterns. Thus, the representation of diazotrophy

315   still appears to warrant further investigation.

Contrary to the original UVic model, we do not apply any explicit growth-rate reduction to the diazotrophs in our OPEM simulations, but we assign a lower nutrient affinity and a higher Fe half-saturation concentration to diazotrophs ($k_{\mathrm{Fe,\,dia}} >$
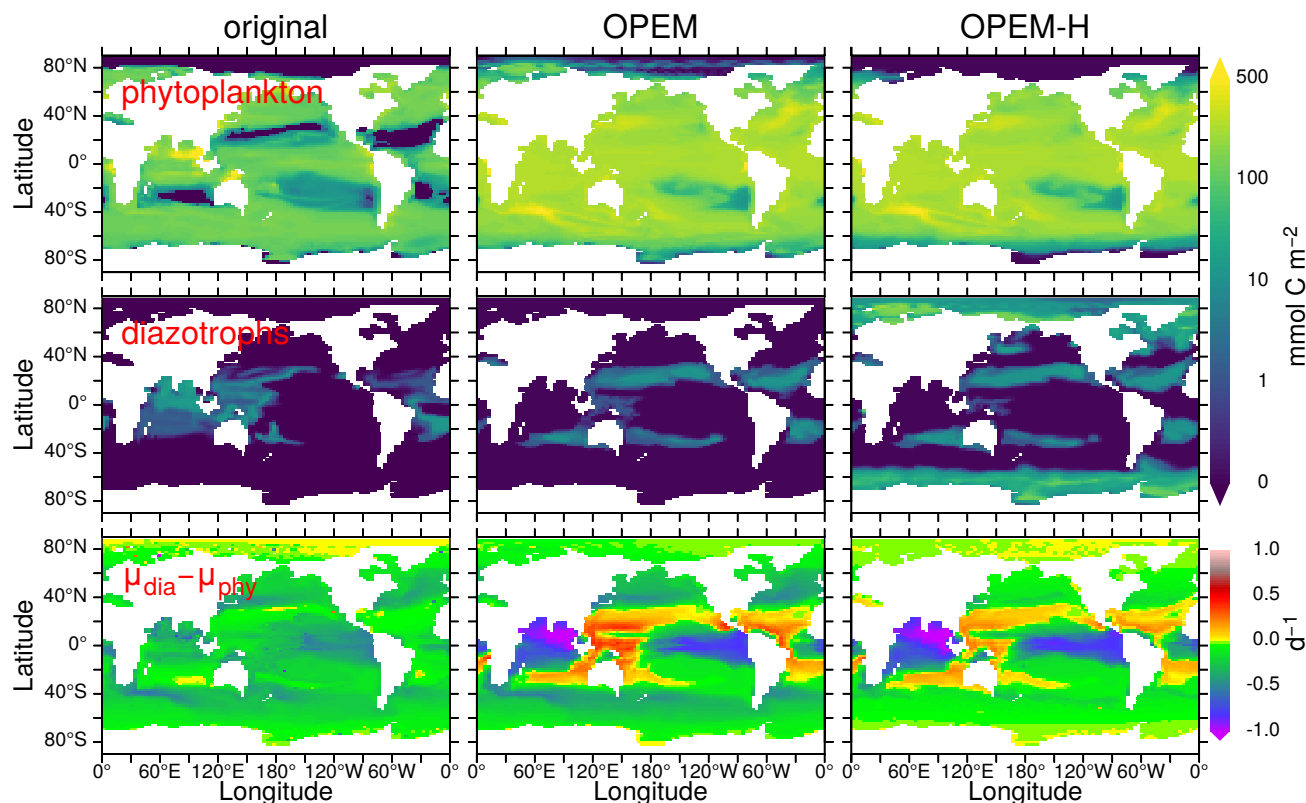
Figure 14. Vertically-integrated and temporally-averaged phytoplankton (top) and diazotroph biomass (centre) and difference between diazotroph and phytoplankton net relative growth rates (bottom), in the original, OPEM, and OPEM-H UVic simulations. Note that the positive growth-rate differences for the original UVic in the Arctic are spurious as they result from $\mu_{\mathrm{dia}} = 0\,\mathrm{d}^{-1}$ and $\mu_{\mathrm{phy}} < 0\,\mathrm{d}^{-1}$

$k_{\mathrm{Fe,\,phy}}$, whereas $k_{\mathrm{Fe,\,dia}} < k_{\mathrm{Fe,\,phy}}$ in the original UVic), and the model calibration yielded a higher values of the prey-capture coefficients for diazotrophs (Table 2, see also Chien et al., 2019). Both OPEM and OPEM-H have a similar phytoplankton biomass and distribution (Fig. 14). Phytoplankton is much more evenly distributed and the integrated biomass is about 2.3 times as large as in the original UVic model.

Diazotrophs are implemented as facultative and their biomass is distributed very differently in all three UVic simulations (Fig. 14). In the original UVic and OPEM, the diazotroph distribution roughly matches that of N_2 fixation, whereas prominent diazotroph biomass appears at high latitudes, even in the Arctic and Antarctic Oceans, in OPEM-H, mostly unassociated with N_2 fixation (cf. Fig. 12). In fact, non-N_2 fixing diazotrophs are responsible for the improved representation of Chl, NPP, and NCP in the Arctic when compared to satellite-based estimates (Figs. 9–11) in OPEM-H, but also for the somewhat higher N* values at high latitudes compared to OPEM (Fig. 5).

The main reason why the facultative diazotrophs can populate the high latitudes in OPEM-H is their higher α (0.5 compared to $0.4\,\mathrm{m}^2\,\mathrm{mol\,C\,W}^{-1}\,(\mathrm{g\,Chl})^{-1}\,\mathrm{d}^{-1}$ for ordinary phytoplankton). A high α for diazotrophs was also obtained by Pahlow et al.

330 (2013). In these areas, characterised by low light and high inorganic nutrient availability, the advantage of a higher α more than compensates for the lower nutrient affinity (A_0) and higher N demand (Q_0^{N}) of the diazotrophs. Our interpretation of this behaviour is that the OPEM models' diazotroph compartment actually represents two functional groups, one occurring in low latitudes, representing what we usually associate with facultative diazotrophs, and one occurring at high latitudes, representing non-N$_2$ fixing species adapted to low light and long periods of darkness. The (facultative) diazotrophs occur mostly where

335 their realised net relative growth rates exceed those of ordinary phytoplankton ($\Delta\mu > 0$, $\Delta\mu = \mu_{\text{dia}} - \mu_{\text{phy}}$) for OPEM and OPEM-H, but not for the original UVic (Fig. 12). The main reason for this discrepancy in the orignal UVic is the much lower food preference for diazotrophs (0.1) compared to ordinary phytoplankton (0.3) in this configuration, which partly decouples the competitive balance between the two autotrophic groups from $\Delta\mu$.

While the occurrence of diazotrophs in the Arctic appears helpful in view of high-latitude NPP, they are also responsible for

340 the overestimation of N* there (Fig. 5), owing to their high N:P ratios. The C:N:P of ordinary phytoplankton in the Arctic (not shown) is close to Redfield proportions in OPEM, but this simulation fails to generate any appreciable NPP there. Although it might also be possible to explain the low N* in the Arctic with a high N:P ratio in Arctic zooplankton, we are not aware of any indication of this. Hence, phytoplankton in the Arctic appears to have a low N:P ratio and cannot be represented by our facultative diazotrophs. Low phytoplankton N:P utilisation ratios in the Arctic have been reported by, e.g., Mills et al.

345 (2015), who also inferred high rates of benthic denitrification there. Since we have no benthic denitrification and almost no N$_2$ fixation in our UVic simulations, it is clear that the stoichiometric imbalance between phytoplankton and zooplankton strongly affect surface N* in the Arctic. Thus, the most likely explanation of the low Arctic N* may be the combination of benthic denitrification and phytoplankton communities dominated by species with high light affinity and a low N subsistence quota.

3.4   C:N:P ratios

350 Simulated log-normally averaged particulate C:N and C:P ratios of both OPEM and OPEM-H are well above the canonical Redfield ratios (C:N = 6.625 mol mol^{-1} and C:P = 106 mol mol^{-1}, Table 3) in the topmost two layers. Both simulations tend to overestimate C:N ratios in the surface layer and underestimate C:P compared to observations compiled by Martiny et al. (2014), though not as much as the uniform Redfield C:P ratio employed in the original UVic model. While the data indicate increasing C:P with depth, it is lower in the second compared to the first layer in OPEM and OPEM-H (Table 3). The increasing

355 C:P in the data may be indicative of preferential remineralisation of P relative to C and N (e.g., Letscher and Moore, 2015), which is absent in the current UVic configurations. The decline of the C:N and C:P with depth in UVic is the result of primary production with lower light and greater nutrient availability in the second layer. This effect may well be too strong in UVic, owing to its coarse vertical resolution, enforcing a homogeneous vertical distribution of all biological tracers within the upper 50 m.

360 The latitudinal patterns of the particulate C:N and C:P ratios are shown in Fig. 15. Interestingly, the simulated C:N ratios are closer to the observations in the southern hemisphere, while the simulated C:P ratios match better in the northern hemisphere. C:N ratios in the surface layer appear too high throughout, whereas those in the second layer are a lot closer to the observations, whereas C:P ratios seem to match similarly in both layers (Table 3 and Fig. 15).

Table 3. Log-normally averaged C:N and C:P ratios for the depth ranges of the upper two layers in the UVic model.

	Martiny et al. (2014)		OPEM		OPEM-H	
	C:N	C:P	C:N	C:P	C:N	C:P
$0 - 50\,\mathrm{m}$	7.6	148	10.0	136	9.7	133
$50 - 130\,\mathrm{m}$	7.4	165	7.7	125	7.4	122

365   Patterns of C:N ratios mirror the relation between light and nutrient limitation in our OPEM simulations, with high C:N ratios indicating strong nutrient limitation, which is also generally observed in phytoplankton culture experiments (Pahlow et al., 2013). Thus, one possible explanation for the too high particulate C:N ratios in the surface layer could be that too little nutrients reach the surface ocean at subtropical northern latitudes. This is consistent with too low rates of NPP being predicted around 20°N (Fig. 10), where the overestimation in surface C:N ratios is strongest (Fig. 15). The lower C:N ratios at high latitudes (60°S and 60°N) in OPEM-H reflect the dominance of (non-N_2 fixing) diazotrophs there in this simulation.

370   The C:N and C:P ratios of sinking particles (detritus) in OPEM and OPEM-H are greater than those of total particulate matter, because a major source of detritus in UVic is zooplankton egestion. Since zooplankton have a C:N:P ratio of 106:16:1 but that of its food is larger, zooplankton respire and egest the excess C in the food, part of which hence ends up in the detritus pool (Fig. 7). The magnitude of this effect is modulated by the zooplankton assimilation efficiency (E_{zoo}) as this determines the fraction of particulate egestion. In regions with high $E_{\mathrm{zoo}} \approx 1$ (Fig. 16), almost no particles are egested, whereas for $E_{\mathrm{zoo}} \approx 0.5$

375   about half of the ingested food (plus excess C) is lost to detritus. The relatively low assimilation efficiencies in the Arctic between 90°E and 120°W in OPEM-H results from the availability of food, as this is the only simulation with any appreciable NPP (Fig. 10) and hence primary-producer biomass in this region (Fig. 14).

4   Conclusions

The above description of the model behaviour highlights some of the improvements of our optimality-based (OPEM, OPEM-

380   H) compared to the original biogeochemistry in the UVic model. Some of these may also be possible with the original UVic with improved parameters, e.g., the deep-ocean N:P distribution (Fig. 8) or a better global NCP (Fig. 11), as these vary strongly among our different parameter sets tested during the calibration process of OPEM and OPEM-H (Chien et al., 2019). Others are simply impossible to reach with a fixed-stoichiometry model, e.g., the distribution of C:N and C:P ratios in particulate matter (Fig. 15). Apparently, our optimality-based biology has a certain internal rigidity (Krishna et al., 2019), preventing

385   us from tuning the OPEM simulations so that, e.g., global NPP, NCP, and N_2-fixation distributions can simultaneously be reproduced very well with the same parameter settings. We thus try to use the resulting, and often systematic, model-data discrepancies in the behaviour of OPEM and OPEM-H as a magnifying glass on model deficiencies to identify avenues for future biogeochemical model development.
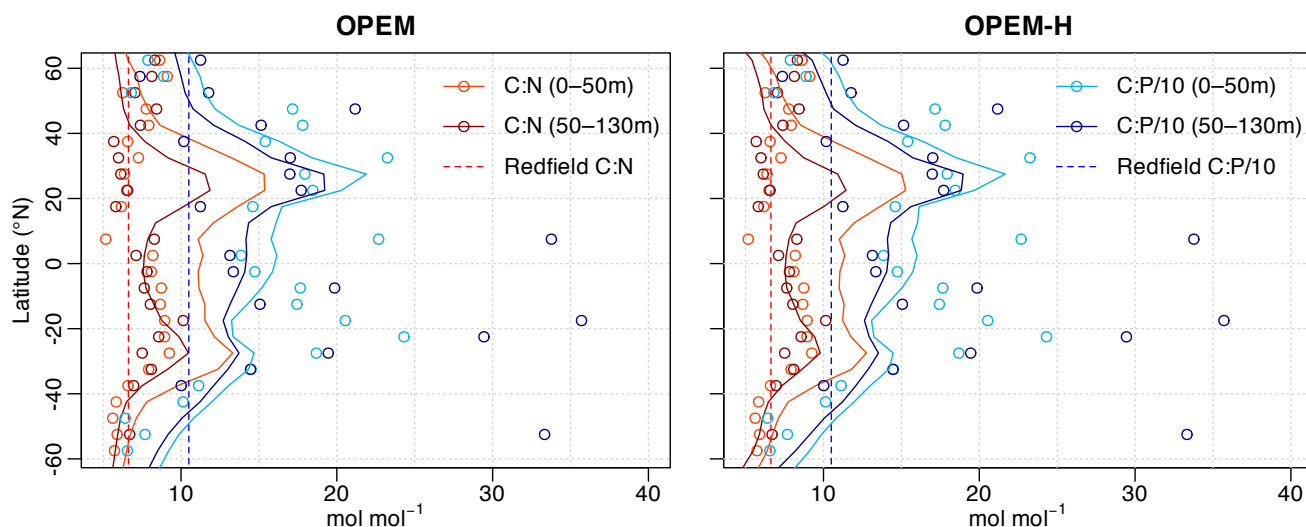
Figure 15. Zonally-averaged particulate C:N and C:P ratios for the depth ranges of the two topmost layers of UVic for 5° latitude bands. Lines are predictions from the OPEM and OPEM-H simulations and circles represent data from Martiny et al. (2014). POC $< 0.01\,\mathrm{mmol\,m^{-3}}$, PON $< 1\,\mu\mathrm{mol\,m^{-3}}$, and POP $< 0.1\,\mu\mathrm{mol\,m^{-3}}$ were removed from the observations prior to calculating the ratios. Observed ratios were mapped onto the UVic grid by taking the median of all available data for each grid cell, and then log-normal zonal averages calculated.

A similar difference in low-latitude NPP pattern as between the CbPM and OPEM predictions can be seen on the Ocean
390   Productivity website (O'Malley, 2017) as resulting from the use of a polynomial (Behrenfeld and Falkowski, 1997) vs. an exponential (Eppley, 1972) temperature function, as also applied in the UVic model. The CbPM does not have a direct temperature dependence and Taucher and Oschlies (2011) found that omission of direct temperature effects on biotic processes did not reduce the ability of the UVic model to reproduce observed tracer distributions. Mechanistically, temperature effects might well be subdued under light-limiting conditions, since photochemical reactions are less temperature sensitive than most other
395   biochemical processes. The wider temperature range for diazotrophy in OPEM-H allows for N_2 fixation north of 40°N, which have been observed recently in the western North Atlantic (Mulholland et al., 2019). Therefore, investigating temperature effects could be a promising approach towards more realistic NPP and N_2-fixation rates.

Environmental constraints on diazotrophy in our UVic simulations suffer from the absence of benthic denitrification, as mentioned above. In addition, preferential P remineralisation could be important for a better representation of N_2 fixation (Monteiro
400   and Follows, 2012). For example, Fernández-Castro et al. (2016) found that preferential P remineralisation is essential for reproducing observed N_2 fixation rates at BATS, particularly when atmospheric deposition of fixed N is also considered. Thus, preferential P remineralisation may not only be important for improving the vertical distribution of particulate C:P (Fig. 15) but also for the simulation of diazotrophy. According to Fernández-Castro et al. (2016), this phenomenon could also be a prerequisite for realistically accounting for the effects of atmospheric deposition of nutrients into the surface ocean.
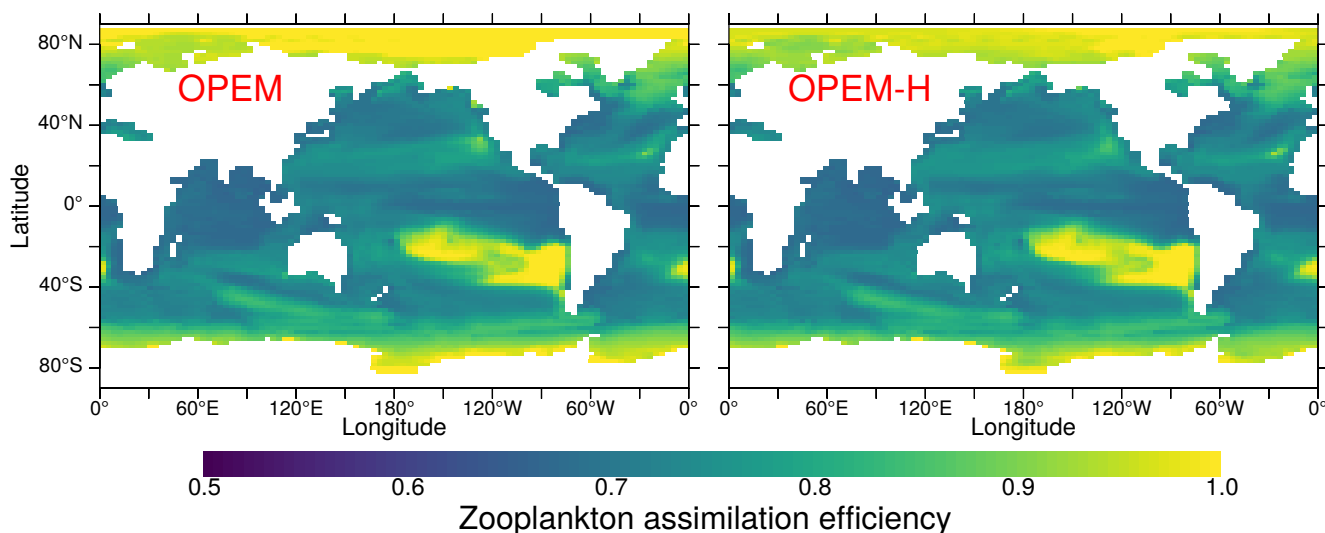
Geoscientific
Model Development
Discussions

Figure 16. Annually-averaged zooplankton assimilation efficiency in the surface layer in the OPEM and OPEM-H simulations.

405   Besides temperature and top-down effects, the distributions of NPP and particulate C:N ratios are also strongly affected by light and nutrient affinity (model parameters α and A_0). The use of fixed settings in these parameters may be responsible for both overestimating NPP at low latitudes (Fig. 10) and preventing ordinary phytoplankton from growing in the Arctic Ocean (Fig. 14), as indicated by the growth of facultative (but mostly non-N_2 fixing) diazotrophs there in the OPEM-H simulation. The biotic compartments of the OPEM configurations have been shown to match the observed behaviour of at least some

410   phytoplankton and zooplankton species (Pahlow and Prowe, 2010; Pahlow et al., 2013). Thus, the failure to obtain a better fit to the observed NPP distribution may reflect a certain rigidity, brought about by attempting to represent plankton communities by a globally uniform parameter set, i.e., one and the same combination of one phytoplankton, one diazotroph, and one zooplankton species. As mentioned above, Arteaga et al. (2016) achieved a strong improvement in model behaviour by replacing α and A_0 with a trade-off represented by opposite linear functions of light and nutrient limitation. Since our cost function does not

415   appear to be very sensitive to α, we interpret these findings as indicating that the regional variability may be more important for the model behaviour than the global average of α. Similar formulations could be introduced, e.g., to represent species sorting (Norberg, 2004; Smith et al., 2016), possibly responsible for regional and local variations in α and A_0. Whether variations in these two parameters suffice, e.g., to explain the low N* in the Arctic, remains to be seen. The approach might have to be extended to further parameters for a more realistic representation of different phytoplankton and zooplankton communities

420   (Prowe et al., 2018; Su et al., 2018). Nevertheless, it is clear from Fig. 5 that N* in the surface ocean is very sensitive to plankton physiology (subsistence quotas), which could greatly complicate inferring regional balances of N_2 fixation and denitrification from N* or similar quantities (e.g., Mills et al., 2015).

Code availability. The University of Victoria Earth System Climate Model version 2.9 is available at http://www.climate.uvic.ca/model/. The code for the Original Model and OPEM is available at https://dx.doi.org/10.3289/SW_1_2020. The instructions needed to reproduce the

425 model results described in this article are in the supplemental material.

Appendix A: Bug fixes applied to all configurations

UVic has already contained code intended to reduce the occurrence of negative concentrations by setting all sink terms to 0 once a concentration drops below a certain threshold. Thus mechanism was made partly ineffective, however, by passing positive values to the biogeochemical subroutine (`npzd_src`), even when the actual tracer concentration was negative, so that

430 the negative concentration was not detected, or too late, and sink terms could still apply. This was corrected by passing the actual tracer values to the `npzd_src` subroutine.

The dynamic Fe model (Nickelsen et al., 2015) injects atmospheric Fe deposition directly into the surface layer, which we consider as bug as this bypasses the surface-flux mechanism built into UVic. Correcting this bug also reduces the occurrence of negative Fe concentrations.

435 ## Appendix B: Optimality-based process descriptions

B1 Phytoplankton and diazotrophs

Please note that we omit the subscripts phy and dia in this subsection.

B1.1 Optimal growth regulation.

Our optimality-based formulations use allocation factors to allocate energy and other resources between light harvesting and

440 nutrient acquisition at each grid point and time step, such that net growth of phytoplankton is maximised. The rates of net relative growth (μ), nutrient uptake (V^N and V^P), and N_2 fixation (F^N) in the OGM are given by the optimality-based chain-model of Pahlow et al. (2013), modified here to allow for temperature dependence and Fe limitation and to avoid out-growing the P subsistence quota during transition towards P limitation. Net relative growth rate is the difference between C fixation (V^C) and the sum of respiration (R) and extra dissolved inorganic C (DIC) release (r_{DIC}, see below) to prevent outgrowing the

445 P subsistence quota. The chain model idea is based on the roles of N and P in a phytoplankton cell, where P is mainly needed for N assimilation and N drives all other biochemical rates (Ågren, 2004), including growth. Thus, the optimal regulation can be described in terms of two conceptual levels, with the lower level consisting of the nutrient-uptake apparatus and the chloroplast, and the upper level being the whole cell. Within the nutrient-uptake apparatus, cellular N is allocated between N and P uptake so as to maximise N assimilation (see Section B1.2 below). Since the role of P is restricted to the nutrient-uptake

Geoscientific
Model Development
Discussions

450 apparatus in this model, we can ignore P in the formulation of the optimal allocation scheme at the whole-cell level:

$$\mu = V^{\mathrm{C}} - R - r_{\mathrm{DIC}} = V^{\mathrm{C}} - R^{\mathrm{Chl}} - \zeta^{\mathrm{N}} V^{\mathrm{N}} - r_{\mathrm{DIC}}, \qquad R = R^{\mathrm{Chl}} + \zeta^{\mathrm{N}} V^{\mathrm{N}} \tag{B1}$$

$$V^{\mathrm{C}} = L_{\mathrm{day}} \cdot V_0^{\mathrm{C}}(T) \cdot f_{\mathrm{C}} \cdot S_I, \qquad R^{\mathrm{Chl}} = [L_{\mathrm{day}} V_0^{\mathrm{C}}(T) \cdot \overline{S}_{\mathrm{I}} + f(T) \cdot R_{\mathrm{M}}^{\mathrm{Chl}}] \cdot \zeta^{\mathrm{Chl}} \cdot \theta \tag{B2}$$

We collect all N-independent gain and loss terms in μ^*,

$$\mu^* = L_{\mathrm{day}} \cdot V_0^{\mathrm{C}}(T) \cdot \overline{S}_{\mathrm{I}} \cdot (1 - \zeta^{\mathrm{Chl}} \hat{\theta}) - f(T) \cdot R_{\mathrm{M}}^{\mathrm{Chl}} \cdot \zeta^{\mathrm{Chl}} \cdot \hat{\theta}, \qquad \hat{\theta} = \frac{\mathrm{Chl{:}C}}{f_{\mathrm{C}}} \tag{B3}$$

455 $$\Rightarrow \qquad \mu = f_{\mathrm{C}} \cdot \mu^* - f_{\mathrm{V}} \cdot \zeta^{\mathrm{N}} \cdot \widehat{V}^{\mathrm{N}} - r_{\mathrm{DIC}}, \qquad f_{\mathrm{C}} = 1 - \frac{1}{2} \frac{Q_0^{\mathrm{N}}}{Q^{\mathrm{N}}} - f_{\mathrm{V}}, \quad f_{\mathrm{V}} = \frac{1}{2} \frac{Q_0^{\mathrm{N}}}{Q^{\mathrm{N}}} - \zeta^{\mathrm{N}} \cdot (Q^{\mathrm{N}} - Q_0^{\mathrm{N}}) \tag{B4}$$

where the allocation factors f_{C} and f_{V} ensure optimal allocation of cellular N between C fixation and nutrient uptake, respectively (see Pahlow et al., 2013, for derivation), $f(T)$ is temperature dependence, L_{day} is day length, V_0^{C} the temperature- and Fe-dependent maximum potential rate for C processing, α the light-absorption coefficient (light affinity), $\hat{\theta}$ the Chl:C ratio of the chloroplast, I irradiance, ζ^{Chl} and ζ^{N} the costs of Chl synthesis and N assimilation, R^{Chl} the cost of Chl synthesis and

460 maintenance, $R_{\mathrm{M}}^{\mathrm{Chl}}$ the cost of Chl maintenance, and $\overline{S}_{\mathrm{I}}$ the depth- and time-averaged light saturation of the photosynthetic apparatus. $\overline{S}_{\mathrm{I}}$ is calculated assuming a triangular light cycle and constant light attenuation within a grid cell:

$$\overline{S}_{\mathrm{I}} = \frac{1}{\Delta z} \int_0^1 \int_0^{\Delta z} 1 - \mathrm{e}^{-\alpha^* \cdot I(z) \cdot x} \mathrm{d}z \mathrm{d}x, \qquad I(z) = I_0 \mathrm{e}^{-\epsilon z}, \qquad \alpha^* = \frac{\alpha \hat{\theta}}{V_0^{\mathrm{C}}(T)} \tag{B5}$$

$$= 1 - \frac{\mathrm{Ei}(-2\alpha^* I_0) - \mathrm{Ei}[-2\alpha^* I(\Delta z)]}{\epsilon \cdot \Delta z} - \frac{(1 - \mathrm{e}^{-2\alpha^* I(\Delta z)})/I(\Delta z) - (1 - \mathrm{e}^{-2\alpha^* I_0})/I_0}{2\alpha^* \cdot \epsilon \cdot \Delta z} \tag{B6}$$

where I_0 and $I(\Delta z)$ are the mean daytime light intensities at the top and bottom of the current grid cell of height Δz, ϵ is

465 the light-attenuation coefficient, Ei is the exponential-integral function, and the factor 2 converts the mean to the maximum irradiance in the triangular light cycle. As in the original UVic code, we assume that $\epsilon \propto \mathrm{N_{phy}} + \mathrm{N_{dia}} + \text{absorption by seawater}$, since chlorophyll is not a tracer. Eqs. (B5) and (B6) apply only for $I > I_{\min}$, where $I_{\min} = \zeta^{\mathrm{Chl}} R_{\mathrm{M}}^{\mathrm{Chl}} f(T)/(\alpha L_{\mathrm{day}})$ is the minimum light intensity for photosynthesis (see Pahlow et al., 2013). Thus, for $I_0 > I_{\min} > I(\Delta z)$, (B6) is applied to the part of the grid-cell where $I > I_{\min}$ and then multiplied with $\Delta z^*/\Delta z$, where $I(\Delta z^*) = I_{\min}$. In effect, this means that $\overline{S}_{\mathrm{I}} > 0$

470 occurs only in the upper 240 m (the top 3 layers) of the Uvic grid.

B1.2 Optimal uptake kinetics.

DIN and DIP uptake and $\mathrm{N_2}$ fixation are defined as products of allocation factors, setting the size of the respective cellular compartment, and the rate of uptake normalized to the size of that compartment ($\widehat{V}$). $\widehat{V}$ is defined in Eq. B8 via optimal uptake kinetics (Pahlow, 2005; Smith et al., 2009). The size of the nutrient-uptake compartment, responsible for DIN and DIP uptake

475 and $\mathrm{N_2}$ fixation, contains fraction f_{V} of the cellular N resources, of which fraction f_{N} is available for DIN uptake, leaving

$f_V(1 - f_N)$ for DIP uptake:

$$V^N = f_V f_N (1 - f_F)\widehat{V}^N, \qquad\qquad V^P = f_V(1 - f_N)\widehat{V}^P, \qquad\qquad F^N = f_V f_N f_F F_0^N(T)\left(1 - \frac{Q_0^P}{Q^P}\right) \quad \text{(B7)}$$

$$\widehat{V}^N = \left(\sqrt{\frac{1}{V_{\max}^N}} + \sqrt{\frac{1}{A_0\,\text{DIN}}}\right)^{-2}, \qquad \widehat{V}^P = \left(\sqrt{\frac{1}{V_0^P(T)}} + \sqrt{\frac{1}{A_0\,\text{DIP}}}\right)^{-2}, \qquad V_{\max}^N = V_0^N(T)\left(1 - \frac{Q_0^P}{Q^P}\right) \quad \text{(B8)}$$

$$f_N = \frac{1}{1 + \sqrt{\dfrac{Q_0^P}{Q^P}\dfrac{V_0^N(T)}{\widehat{V}^P}\left(\dfrac{\widehat{V}^N}{V_{\max}^N}\right)^{1.5}}}, \qquad f_F = \begin{cases} 1 & \text{if} \quad V^N(f_F = 0) < F^N(f_F = 1) \\ 0 & \text{if} \quad V^N(f_F = 0) \geq F^N(f_F = 1) \end{cases} \quad \text{(B9)}$$

where A_0 is nutrient affinity and f_F the allocation for N_2 fixation within the nutrient-uptake compartment. The allocation factor f_F is implemented as a switch, so that the facultative diazotrophs either fix N_2 or utilize DIN (see Pahlow et al., 2013, for derivation). The dependence of $V_{\max}$ and F^N on Q^P introduces a chain of limitations, where the P quota limits N uptake and N limits all other processes. Extra DIC release (r_{DIC}) during transition towards severe P limitation prevents outgrowing of the P subsistence quota (Q_0^P):

$$r_{DIC} = \max\left[(V^C - R)\frac{Q_0^P}{Q^P} - \frac{V^P}{Q_0^P}, 0\right] \cdot \max\left(2 - \frac{Q^P}{Q_0^P}, 0\right) \quad \text{(B10)}$$

Eq. (B10) is an admittedly rather arbitrary measure to stabilise the OGM, but it did result in reasonable rates of DOC production in a previous study (Fernández-Castro et al., 2016).

B1.3 Temperature and Fe limitation

Temperature and Fe limitation are implemented by

$$V_0^C(T) = V_0^N(T) = f_p(T) \cdot S_{Fe} \cdot V_0, \qquad V_0^P(T) = f_p(T) \cdot V_0, \qquad F_0^N(T) = f_{nfix}(T) \cdot S_{Fe} \cdot F_0 \qquad p \in \{\text{phy, dia}\} \quad \text{(B11)}$$

$$\lambda_{phy} = \lambda_{0,phy} \cdot f_{phy}(T) \qquad M_{dia} = M_{0,dia} \cdot f_{dia}(T) \quad \text{(B12)}$$

where V_0 is the potential-rate parameter, F_0 the potential rate of N_2 fixation, $f_p(T)$ the group-specific temperature dependence of nutrient uptake and photosynthesis, $f_{dia}(T)$ the temperature dependence of N_2 fixation and S_{Fe} the Fe limitation term.

B2 Zooplankton

495 Net growth (μ_{zoo}) is described in terms of total ($\mathcal{A}_\mathrm{t}$, see Eq. (B18) below) and foraging activity ($\mathcal{A}_\mathrm{f}$), and corrected for r_Q:

$$\mu_{\mathrm{zoo}} = (E_{\mathrm{zoo}} \cdot g_{\mathrm{zoo}} - R^*_{\mathrm{zoo}}) \cdot r_\mathrm{Q}, \qquad\qquad g_{\mathrm{zoo}} = \mathcal{A}_\mathrm{f} \cdot S_\mathrm{g}, \quad S_\mathrm{g} = 1 - \exp(-\Pi^\mathrm{C}) \tag{B13}$$

$$E_{\mathrm{zoo}} = E_{\max}\left[1 - \exp\left(\frac{\mathcal{A}_\mathrm{t}}{\mathcal{A}_\mathrm{f}} - \beta\right)\right], \qquad\qquad X^\mathrm{C}_{\mathrm{zoo}} = g_{\mathrm{zoo}}(1 - E_{\mathrm{zoo}}) \cdot \mathrm{C}_{\mathrm{zoo}}, \quad X^n_{\mathrm{zoo}} = R^n_{\mathrm{zoo}} \cdot \frac{X^\mathrm{C}_{\mathrm{zoo}}}{R^\mathrm{C}_{\mathrm{zoo}}} \tag{B14}$$

$$R^*_{\mathrm{zoo}} = c_\mathrm{a} \cdot E_{\mathrm{zoo}} \cdot g_{\mathrm{zoo}} + c_\mathrm{f} \cdot \mathcal{A}_\mathrm{f} + f_{\mathrm{zoo}}(T) \cdot R^\mathrm{M}_{\mathrm{zoo}}, \qquad\qquad R^\mathrm{C}_{\mathrm{zoo}} = (E_{\mathrm{zoo}} \cdot g_{\mathrm{zoo}} - \mu_{\mathrm{zoo}}) \cdot \mathrm{C}_{\mathrm{zoo}} \tag{B15}$$

$$R^n_{\mathrm{zoo}} = \frac{g_{\mathrm{zoo}} \cdot \mathrm{C}_{\mathrm{zoo}} \cdot \dfrac{\Pi^n}{\Pi^\mathrm{C}} - \mu_{\mathrm{zoo}} \cdot n_{\mathrm{zoo}}}{1 + \dfrac{X^\mathrm{C}_{\mathrm{zoo}}}{R^\mathrm{C}_{\mathrm{zoo}}}}, \quad n \in \{\mathrm{N, P}\} \tag{B16}$$

500 where $\mathrm{C}_{\mathrm{zoo}} = 6.625 \cdot \mathrm{N}_{\mathrm{zoo}}$ and $\mathrm{N}_{\mathrm{zoo}}$ are zooplankton POC and PON, μ_{zoo} net relative growth rate, $G^\mathrm{N}_{\mathrm{zoo}}$ predation on zooplankton, M_{zoo} (quadratic) mortality, $Q^\mathrm{N}_{\mathrm{zoo}}$ N:C ratio, g_{zoo} relative ingestion rate, E_{zoo} and $E_{\max}$ actual and maximal assimilation efficiency, $X^\mathrm{C}_{\mathrm{zoo}}$ egestion, R^*_{zoo} and $R^\mathrm{C}_{\mathrm{zoo}}$ minimal (uncorrected for r_Q) and actual respiration, R^n_{zoo} metabolic N and P losses, β digestion coefficient, c_a and c_f cost of assimilation and foraging coefficients, and $R^\mathrm{M}_{\mathrm{zoo}}$ maintenance respiration. The same relation between dissolved and particulate losses applies for N and P as for C in (B16). Eqs. (B13)–(B15) define the benefits

505 (g_{zoo}) and costs (E_{zoo} and R^*_{zoo}) of foraging, whence the optimal foraging activity is obtained as

$$\mathcal{A}_\mathrm{f} = \begin{cases} \dfrac{\mathcal{A}_\mathrm{t}}{-1 - W_{-1}\left(\left[\dfrac{c_\mathrm{f}}{S_\mathrm{g} E_{\max}(1 - c_\mathrm{a})} - 1\right] \mathrm{e}^{-(1+\beta)}\right)} & \text{if } \Pi^\mathrm{C} > \Pi_{\mathrm{th}} \\ 0 & \text{if } \Pi^\mathrm{C} \leq \Pi_{\mathrm{th}} \end{cases}, \qquad \Pi_{\mathrm{th}} = \ln \frac{1}{1 - \dfrac{c_\mathrm{f}}{E_{\max}(1 - c_\mathrm{a})}} \tag{B17}$$

where W_{-1} is Lambert's W-function and Π_{th} is the feeding threshold. $\mathcal{A}_\mathrm{t}$ is a function of the maximal ingestion rate ($g_{\max}$) and temperature:

$$\mathcal{A}_\mathrm{t} = g_{\max} \cdot f_{\mathrm{zoo}}(T)\left\{-1 - W_{-1}\left(\left[\frac{c_\mathrm{f}}{E_{\max}(1 - c_\mathrm{a})} - 1\right] \mathrm{e}^{-(1+\beta)}\right)\right\} \tag{B18}$$

510 The predation rates for individual prey types are

$$G^\mathrm{C}_p = \frac{\phi_p \mathrm{C}_p}{\Pi^\mathrm{C}} \cdot g_{\mathrm{zoo}} \cdot \mathrm{C}_{\mathrm{zoo}}, \qquad \mathrm{C}_{\mathrm{zoo}} = \frac{\mathrm{N}_{\mathrm{zoo}}}{Q^\mathrm{N}_{\mathrm{zoo}}}, \qquad G^\mathrm{N}_p = G^\mathrm{C}_p \cdot Q^\mathrm{N}_p, \qquad G^\mathrm{P}_p = G^\mathrm{C}_p \cdot Q^\mathrm{P}_p, \qquad p \in \{\mathrm{phy, dia, det, zoo}\} \tag{B19}$$

Eqs. (4) and (B13)–(B16) stipulate that most of the excess C, N, or P rejected to maintain homeostasis is released in dissolved inorganic form (cf. Eqs. B13 and B15). This is because the actual growth rate μ_{zoo} is obtained as the product of r_Q and the potential growth rate, i.e., that obtained for food with the same stoichiometry as the zooplankton in Eq. (B13), and respiration

515 $R^\mathrm{C}_{\mathrm{zoo}}$ is then derived from μ_{zoo} in Eq. (B15), whereas egestion $X^\mathrm{C}_{\mathrm{zoo}}$ is not affected by r_Q in Eq. (B13). Since the relation of dissolved and particulate N and P losses follows that for C (X^n_{zoo} in Eq. B13), a stoichiometric imbalance between zooplankton and its food increases dissolved losses for N and P as well.

Author contributions. L. Arteaga and M. Pahlow implemented the optimality-based formulations in the UVic. M. Pahlow and C.-T. Chien performed the ensemble solutions and selected the reference simulations. All authors contributed to the manuscript text.

520 *Competing interests.* The authors declare that they have no conflict of interest.

References

Ågren, G. I.: The C : N : P stoichiometry of autotrophs – theory and observations, Ecol. Lett., 7, 185–191, https://doi.org/10.1111/j.1461-0248.2004.00567.x, 2004.

Anderson, L. A. and Sarmiento, J. L.: Redfield ratios of remineralization determined by nutrient data analysis, Global Biogeochem. Cycles, 8, 65–80, https://doi.org/10.1029/93GB03318, 1994.

Arteaga, L., Pahlow, M., and Oschlies, A.: Global patterns of phytoplankton nutrient and light colimitation inferred from an optimality-based model, Global Biogeochem. Cycles, 28, https://doi.org/10.1002/2013GB004668, 2014.

Arteaga, L., Pahlow, M., and Oschlies, A.: Modelled Chl:C ratio and derived estimates of phytoplankton carbon biomass and its contribution to total particulate organic carbon in the global surface ocean, Global Biogeochem. Cycles, 30, https://doi.org/10.1002/2016GB005458, 2016.

Behrenfeld, M. J. and Falkowski, P. G.: Photosynthetic rates derived from satellite-based chlorophyll concentration, Limnol. Oceanogr., 42, 1–20, https://doi.org/10.4319/lo.1997.42.1.0001, 1997.

Carr, M.-E., Friedrichs, M. A., Schmeltz, M., Noguchi Aita, M., Antoine, D., Arrigo, K. R., Asanuma, I., Aumont, O., Barber, R., Behrenfeld, M., et al.: A comparison of global estimates of marine primary production from ocean color, Deep-Sea Res. II, 53, 741–770, https://doi.org/10.1016/j.dsr2.2006.01.028, 2006.

Chen, B. and Smith, S. L.: Optimality-based approach for computationally efficient modeling of phytoplankton growth, chlorophyll-to-carbon, and nitrogen-to-carbon ratios, Ecol. Model., 385, 197–212, https://doi.org/10.1016/j.ecolmodel.2018.08.001, 2018.

Chien, C.-T., Pahlow, M., Schartau, M., and Oschlies, A.: Optimality-Based Non-Redfield Ecosystem Model in the UVic-ESCM. Part II: Sensitivity Analysis and Model Calibration, Geosci. Model Dev. Discuss., submitted, 2019.

Deutsch, C., Sarmiento, J. L., Sigman, D. M., Gruber, N., and Dunne, J. P.: Spatial coupling of nitrogen inputs and losses in the ocean, Nature, 445, 163–167, https://doi.org/10.1038/nature05392, 2007.

DeVries, T. and Weber, T.: The export and fate of organic matter in the ocean: New constraints from combining satellite and oceanographic tracer observations, Global Biogeochem. Cycles, 31, 535–555, https://doi.org/10.1002/2016GB005551, 2017.

Dunne, J. P., Armstrong, R. A., Gnanadesikan, A., and Sarmiento, J. L.: Empirical and mechanistic models for the particle export ratio, Global Biogeochem. Cycles, 19, GB4026, https://doi.org/10.1029/2004GB002390, 2005.

Eby, M., Zickfeld, K., Montenegro, A., Archer, D., Meissner, K. J., and Weaver, A. J.: Lifetime of Anthropogenic Climate Change: Millennial Time Scales of Potential CO_2 and Surface Temperature Perturbations, J. Clim., 22, 2501–2511, https://doi.org/10.1175/2008JCLI2554.1, 2009.

Eby, M., Weaver, A. J., Alexander, K., Zickfeld, K., Abe-Ouchi, A., Cimatoribus, A. A., Crespin, E., Drijfhout, S. S., Edwards, N. R., Eliseev, A. V., Feulner, G., Fichefet, T., Forest, C. E., Goosse, H., Holden, P. B., Joos, F., Kawamiya, M., Kicklighter, D., Kienert, H., Matsumoto, K., Mokhov, I. I., Monier, E., Olsen, S. M., Pedersen, J. O. P., Perrette, M., Philippon-Berthier, G., Ridgwell, A., Schlosser, A., von Deimling, T. S., Shaffer, G., Smith, R. S., Spahni, R., Sokolov, A. P., Steinacher, M., Tachiiri, K., Tokos, K., Yoshimori, M., Zeng, N., and Zhao, F.: Historical and idealized climate model experiments: an intercomparison of Earth system models of intermediate complexity, Clim. Past, 9, 1111–1140, https://doi.org/10.5194/cp-9-1111-2013, 2013.

Eppley, R. W.: Temperature and phytoplankton growth in the sea, Fish. Bull., 70, 1063–1085, 1972.

Fernández-Castro, B., Pahlow, M., Mouriño-Carballido, B., Marañón, E., and Oschlies, A.: Optimality-based *Trichodesmium* Diazotrophy in the North Atlantic Subtropical Gyre, J. Plankton Res., 38, 946–963, https://doi.org/10.1093/plankt/fbw047, 2016.

Garcia, H. E., Locarnini, R. A., Boyer, T. P., Antonov, J. I., Mishonov, A. V., Baranova, O. K., Zweng, M. M., Reagan, J. R., and Johnson, D. R.: Dissolved Oxygen, Apparent Oxygen Utilization, and Oxygen Saturation, in: World Ocean Atlas 2013, edited by Levitus, S., vol. 3, NOAA Atlas NESDIS 75, https://doi.org/http://www.nodc.noaa.gov/OC5/indprod.html, 2013a.

Garcia, H. E., Locarnini, R. A., Boyer, T. P., Antonov, J. I., Mishonov, A. V., Baranova, O. K., Zweng, M. M., Reagan, J. R., and Johnson, D. R.: Dissolved Inorganic Nutrients (phosphate, nitrate, silicate), in: World Ocean Atlas 2013, edited by Levitus, S., vol. 4, NOAA Atlas NESDIS 76, https://doi.org/http://www.nodc.noaa.gov/OC5/indprod.html, 2013b.

Getzlaff, J. and Dietze, H.: Effects of increased isopycnal diffusivity mimicking the unresolved equatorial intermediate current system in an earth system climate model, Geophys. Res. Lett., 40, 2166–2170, https://doi.org/10.1002/grl.50419, 2013.

Gismervik, I.: Numerical and functional responses of choreo- and oligotrich planktonic ciliates, Aquat. Microb. Ecol., 40, 163–173, https://doi.org/10.3354/ame040163, 2005.

Gruber, N.: The dynamics of the marine nitrogen cycle and its influence on atmospheric CO_2 variations, in: The Ocean Carbon Cycle and Climate, edited by Follows, M. and Oguz, T., pp. 97–148, Kluwer, 2004.

Gruber, N. and Sarmiento, J. L.: Global Patterns of marine nitrogen fixation and denitrification, Global Biogeochem. Cycles, 11, 235–266, https://doi.org/10.1029/97GB00077, 1997.

Holling, C. S. and Buckingham, S.: A behavioral model of predator-prey functional responses, Behav. Sci., 21, 183–195, https://doi.org/10.1002/bs.3830210305, 1976.

Houlton, B. Z., Wang, Y.-P., Vitousek, P. M., and Field, C. B.: A unifying framework for dinitrogen fixation in the terrestrial biosphere, Nature, 454, 327–330, https://doi.org/10.1038/nature07028, 2008.

Hu, C., Lee, Z., and Franz, B.: Chlorophyll a algorithms for oligotrophic oceans: A novel approach based on three-band reflectance difference, J. Geophys. Res. Oceans, 117, https://doi.org/10.1029/2011jc007395, 2012.

Hülse, D., Arndt, S., Wilson, J. D., Munhoven, G., and Ridgwell, A.: Understanding the causes and consequences of past marine carbon cycling variability through models, Earth Sci. Rev., 171, 349–382, https://doi.org/10.1016/j.earscirev.2017.06.004, 2017.

IPCC: Climate Change 2013: The Physical Science Basis. Contribution of Working Group I to the Fifth Assessment Report of the Intergovernmental Panel on Climate Change, Cambridge, 2013.

Keller, D. P., Oschlies, A., and Eby, M.: A new marine ecosystem model for the University of Victoria Earth System Climate Model, Geosci. Model Dev., 5, 1195–1220, https://doi.org/10.5194/gmd-5-1195-2012, 2012.

Keller, D. P., Lenton, A., Scott, V., Vaughan, N. E., Bauer, N., Ji, D., Jones, C. D., Kravitz, B., Muri, H., and Zickfeld, K.: The Carbon Dioxide Removal Model Intercomparison Project (CDRMIP): rationale and experimental protocol for CMIP6, Geosci. Model Dev., 11, 1133–1160, https://doi.org/10.5194/gmd-11-1133-2018, 2018.

Key, R., Olsen, A., van Heuven, S., Lauvset, S. K., Velo, A., Lin, X., Schirnick, C., Kozyr, A., Tanhua, T., Hoppema, M., Jutterström, S., Steinfeldt, R., Jeansson, E., Ishi, M., Perez, F. F., and Suzuki, T.: Global Ocean Data Analysis Project, Version 2 (GLODAPv2), ORNL/CDIAC-162, NDP-P093, Carbon Dioxide Information Analysis Center, Oak Ridge National Laboratory, US Department of Energy, https://doi.org/10.3334/CDIAC/OTG.NDP093_GLODAPv2, 2015.

Kiørboe, T., Møhlenberg, F., and Hamburger, K.: Bioenergetics of the planktonic copepod *Acartia tonsa*: relation between feeding, egg production and respiration, and composition of specific dynamic action, Mar. Ecol. Prog. Ser., 26, 85–97, https://doi.org/10.3354/meps026085, 1985.

Klausmeier, C. A., Litchman, E., Daufresne, T., and Levin, S. A.: Phytoplankton stoichiometry, Ecol. Res., 23, 479–485, https://doi.org/10.1007/s11284-008-0470-8, 2008.

Kriest, I.: Calibration of a simple and a complex model of global marine biogeochemistry, Biogeosciences, 14, 4965–4984, https://doi.org/10.5194/bg-14-4965-2017, 2017.

Krishna, S., Pahlow, M., and Schartau, M.: Comparison of two carbon-nitrogen regulatory models calibrated with mesocosm data, Ecol. Model., https://doi.org/10.1016/j.ecolmodel.2019.05.016, 2019.

605 Kvale, K. F., Khatiwala, S., Dietze, H., Kriest, I., and Oschlies, A.: Evaluation of the Transport Matrix Method for simulation of ocean biogeochemical tracers, Geosci. Model Dev., 10, 2425–2445, https://doi.org/10.5194/gmd-10-2425-2017, 2017.

Kwiatkowski, L., Aumont, O., Bopp, L., and Ciais, P.: The Impact of Variable Phytoplankton Stoichiometry on Projections of Primary Production, Food Quality, and Carbon Uptake in the Global Ocean, Global Biogeochem. Cycles, 32, https://doi.org/10.1002/2017gb005799, 2018.

610 Landolfi, A., Dietze, H., Koeve, W., and Oschlies, A.: Overlooked runaway feedback in the marine nitrogen cycle: the vicious cycle, Biogeosciences, 10, 1351–1363, https://doi.org/10.5194/bg-10-1351-2013, 2013.

Landolfi, A., Kaehler, P., Koeve, W., and Oschlies, A.: Global Marine N_2 Fixation Estimates: From Observations to Models, Front. Microbiol., 9, 2112, https://doi.org/10.3389/fmicb.2018.02112, 2018.

Laufkötter, C., Vogt, M., Gruber, N., Aita-Noguchi, M., Aumont, O., Bopp, L., Buitenhuis, E., Doney, S. C., Dunne, J., Hashioka, T., Hauck,
615 J., Hirata, T., John, J., Quéré, C. L., Lima, I. D., Nakano, H., Seferian, R., Totterdell, I., Vichi, M., and Völker, C.: Drivers and uncertainties of future global marine primary production in marine ecosystem models, Biogeosciences, 12, 6955–6984, https://doi.org/10.5194/bg-12-6955-2015, 2015.

Lauvset, S. K., Key, R. M., Olsen, A., van Heuven, S., Velo, A., Lin, X., Schirnick, C., Kozyr, A., Tanhua, T., Hoppema, M., Jutterström, S., Steinfeldt, R., Jeansson, E., Ishii, M., Pérez, F. F., Suzuki, T., and Watelet, S.: A new global interior ocean mapped climatology: the
620 $1° × 1°$ GLODAP version 2, Earth Syst. Sci. Data, 8, 325–340, https://doi.org/10.5194/essd-8-325-2016, 2016.

Laws, E. A., Falkowski, P. G., Walker O. Smith, J., Ducklow, H., and McCarthy, J. J.: Temperature effects on export production in the open ocean, Global Biogeochem. Cycles, 14, 1231–1246, https://doi.org/10.1029/1999GB001229, 2000.

Lessard, E. J. and Murrell, M. C.: Microzooplankton herbivory and phytoplankton growth in the northwestern Sargasso Sea, Aquat. Microb. Ecol., 16, 173–188, https://doi.org/10.3354/ame016173, 1998.

625 Letscher, R. T. and Moore, J. K.: Preferential remineralization of dissolved organic phosphorus and non-Redfield DOM dynamics in the global ocean: Impacts on marine productivity, nitrogen fixation, and carbon export, Global Biogeochem. Cycles, 29, 2014GB004904, https://doi.org/10.1002/2014GB004904, 2015.

Li, Z. and Cassar, N.: Satellite estimates of net community production based on O_2/Ar observations and comparison to other estimates, Global Biogeochem. Cycles, 30, 2015GB005314, https://doi.org/10.1002/2015GB005314, 2016.

630 Löptien, U. and Dietze, H.: Effects of parameter indeterminacy in pelagic biogeochemical modules of Earth System Models on projections into a warming future: the scale of the problem, Global Biogeochem. Cycles, 31, https://doi.org/10.1002/2017GB005690, 2017.

Löscher, C. R., Mohr, W., Bange, H. W., and Canfield, D. E.: No nitrogen fixation in the Bay of Bengal?, Biogeosciences Discuss., 2019, 1–25, https://doi.org/10.5194/bg-2019-347, 2019.

Luo, Y.-W., Doney, S. C., Anderson, L. A., Benavides, M., Berman-Frank, I., Bode, A., Bonnet, S., Boström, K. H., Böttjer, D., Capone,
635 D. G., Carpenter, E. J., Chen, Y. L., Church, M. J., Dore, J. E., Falcón, L. I., Fernández, A., Foster, R. A., Furuya, K., Gómez, F., Gundersen, K., Hynes, A. M., Karl, D. M., Kitajima, S., Langlois, R. J., LaRoche, J., Letelier, R. M., Marañón, E., McGillicuddy Jr., D. J., Moisander, P. H., Moore, C. M., Mouriño-Carballido, B., Mulholland, M. R., Needoba, J. A., Orcutt, K. M., Poulton, A. J., Rahav, E., Raimbault, P., Rees, A. P., Riemann, L., Shiozaki, T., Subramaniam, A., Tyrrell, T., Turk-Kubo, K. A., Varela, M., Villareal, T. A., Webb, E. A., White,

A. E., Wu, J., and Zehr, J. P.: Database of diazotrophs in global ocean: abundance, biomass and nitrogen fixation rates, Earth Syst. Sci.

640   Data, 4, 47–73, https://doi.org/10.5194/essd-4-47-2012, 2012.

Martiny, A. C., Vrugt, J. A., and Lomas, M. W.: Concentrations and ratios of particulate organic carbon, nitrogen, and phosphorus in the
global ocean, Sci. Data, 1, 140048, https://doi.org/10.1038/sdata.2014.48, 2014.

Matrai, P. A. and Keller, M. D.: Total organic sulfur and dimethylsulfoniopropionate in marine phytoplankton: intracellular variations, Mar.
Biol., 119, 61–68, https://doi.org/10.1007/BF00350107, 1994.

645   Millero, F. J., Fiol, S., Campbell, D. M., and Parilla, G.: Carbon dioxide, hydrographic, and chemical data obtained during the R/V Hespérides
cruise in the Atlantic Ocean (WOCE section A5, July 14 – August 15, 1992), Carbon Dioxide Information Analysis Center, Oak Ridge
National Laboratory, U.S. Department of Energy, https://doi.org/10.3334/CDIAC/otg.ndp074, 2000.

Mills, M. M., Brown, Z. W., Lowry, K. E., van Dijken, G. L., Becker, S., Pal, S., Benitez-Nelson, C. R., Downer, M. M., Strong, A. L., Swift,
J. H., Pickart, R. S., and Arrigo, K. R.: Impacts of low phytoplankton NO_3^-:PO_4^{3-} utilization ratios over the Chukchi Shelf, Arctic Ocean,

650   Deep-Sea Res. II, 118, 105–121, https://doi.org/10.1016/j.dsr2.2015.02.007, 2015.

Monteiro, F. M. and Follows, M. J.: On nitrogen fixation and preferential remineralization of phosphorus, Geophys. Res. Lett., 39, L06607,
https://doi.org/10.1029/2012GL050897, 2012.

Monteiro, F. M., Dutkiewicz, S., and Follows, M. J.: Biogeographical controls on the marine nitrogen fixers, Global Biogeochem. Cycles,
25, GB2003, https://doi.org/10.1029/2010GB003902, 2011.

655   Mulholland, M. R., Bernhardt, P. W., Widner, B. N., Selden, C. R., Chappell, P. D., Clayton, S., Mannino, A., and Hyde, K.: High Rates of
N_2 Fixation in Temperate, Western North Atlantic Coastal Waters Expand the Realm of Marine Diazotrophy, Global Biogeochem. Cycles,
33, https://doi.org/10.1029/2018gb006130, 2019.

Nickelsen, L., Keller, D. P., and Oschlies, A.: A dynamic marine iron cycle module coupled to the University of Victoria Earth System Model:
the Kiel Marine Biogeochemical Model 2 for UVic 2.9, Geosci. Model Dev., 8, 1357–1381, https://doi.org/10.5194/gmd-8-1357-2015,

660   2015.

Niemeyer, D., Kemena, T. P., Meissner, K. J., and Oschlies, A.: A model study of warming-induced phosphorus–oxygen feedbacks in open-
ocean oxygen minimum zones on millennial timescales, Earth Syst. Dynam., 8, 357–367, https://doi.org/10.5194/esd-8-357-2017, 2017.

Norberg, J.: Biodiversity and ecosystem functioning: A complex adaptive systems approach, Limnol. Oceanogr., 49, 1269–1277,
https://doi.org/10.4319/lo.2004.49.4_part_2.1269, 2004.

665   O'Malley, R.: Ocean Productivity, http://www.science.oregonstate.edu/ocean.productivity/index.php, 2017.

Oschlies, A., Koeve, W., and Garçon, V.: An Eddy-Permitting Coupled Physical-Biological Model of the North Atlantic 2. Ecosystem
Dynamics and Comparison With Satellite and JGOFS Local Studies Data, Global Biogeochem. Cycles, 14, 499–523, 2000.

Oschlies, A., Duteil, O., Getzlaff, J., Koeve, W., Landolfi, A., and Schmidtko, S.: Patterns of deoxygenation: sensitivity to natural and
anthropogenic drivers, Phil. Trans. R. Soc. Lond. A, 375, 20160325, https://doi.org/10.1098/rsta.2016.0325, 2017.

670   Pahlow, M.: Linking chlorophyll-nutrient dynamics to the Redfield N:C ratio with a model of optimal phytoplankton growth, Mar. Ecol.
Prog. Ser., 287, 33–43, https://doi.org/10.3354/meps287033, 2005.

Pahlow, M. and Prowe, A. E. F.: Model of optimal current feeding in zooplankton, Mar. Ecol. Prog. Ser., 403, 129–144,
https://doi.org/10.3354/meps08466, 2010.

Pahlow, M., Dietze, H., and Oschlies, A.: Optimality-based model of phytoplankton growth and diazotrophy, Mar. Ecol. Prog. Ser., 489,

675   1–16, https://doi.org/10.3354/meps10449, 2013.

Park, J.-Y., Stock, C. A., Dunne, J. P., Yang, X., and Rosati, A.: Seasonal to multiannual marine ecosystem prediction with a global Earth system model, Science, 365, 284–288, https://doi.org/10.1126/science.aav6634, 2019.

Prowe, A. E. F., Visser, A. W., Andersen, K. H., Chiba, S., and Kiørboe, T.: Biogeography of zooplankton feeding strategy, Limnol. Oceanogr., 64, 661–678, https://doi.org/10.1002/lno.11067, 2018.

680 Smith, S. L., Yamanaka, Y., Pahlow, M., and Oschlies, A.: Optimal uptake kinetics: physiological acclimation explains the pattern of nitrate uptake by phytoplankton in the ocean, Mar. Ecol. Prog. Ser., 384, 1–12, 2009.

Smith, S. L., Pahlow, M., Merico, A., Acevedo-Trejos, E., Sasai, Y., Yoshikawa, C., Sasaoka, K., Fujiki, T., Matsumoto, K., and Honda, M. C.: Flexible phytoplankton functional type (FlexPFT) model: size-scaling of traits and optimal growth, J. Plankton Res., 38, 977–992, https://doi.org/10.1093/plankt/fbv038, 2016.

685 Strom, S. L.: Growth and grazing rates of the herbivorous dinoflagellate *Gymnodinium* sp. from the open subarctic Pacific Ocean, Mar. Ecol. Prog. Ser., 78, 103–113, https://doi.org/10.3354/meps078103, 1991.

Strom, S. L., Miller, C. B., and Frost, B. W.: What sets the lower limit to phytoplankton stocks in high-nitrate, low-chlorophyll regions of the open ocean?, Mar. Ecol. Prog. Ser., 193, 19–31, https://doi.org/10.3354/meps193019, 2000.

Su, B., Pahlow, M., and Prowe, F.: The role of microzooplankton trophic interactions in modelling a suite of mesocosm ecosystems, Ecol.
690   Model., 368, 169–179, https://doi.org/10.1016/j.ecolmodel.2017.11.013, 2018.

Taucher, J. and Oschlies, A.: Can we predict the direction of marine primary production change under global warming?, Geophys. Res. Lett., 38, L02603, https://doi.org/10.1029/2010GL045934, 2011.

Wang, W.-L., Moore, J. K., Martiny, A. C., and Primeau, F. W.: Convergent estimates of marine nitrogen fixation, Nature, 566, 205–211, https://doi.org/10.1038/s41586-019-0911-2, 2019.

695 Weaver, A., Eby, M., Wiebe, E., Bitz, C., Duffy, P., Ewen, T., Fanning, A., Holland, M., MacFadyen, A., Matthews, H., Meissner, K., Saenko, O., Schmittner, A., Wang, H., and Yoshimori, M.: The UVic Earth System Climate Model: Model description, climatology, and applications to past, present and future climates, Atmos.-Ocean, 39, 361–428, https://doi.org/10.1080/07055900.2001.9649686, 2001.

Westberry, T., Behrenfeld, M. J., Siegel, D. A., and Boss, E.: Carbon-based primary productivity modeling with vertically resolved photoac-climation, Global Biogeochem. Cycles, 22, GB2024, https://doi.org/10.1029/2007GB003078, 2008.